Power System Applications of Fiber Optic Sensors

A. R. Johnston
S. P. Jackson
H. Kirkham
C. Yeh

June 1986

ABSTRACT

This document is a progress report of work done in 1985 on the Communications and Control for Electric Power Systems Project at the Jet Propulsion Laboratory. Three topics are covered: Electric Field Measurement, Fiber Optic Temperature Sensing, and Optical Power Transfer.

Work was done on the measurement of ac and dc electric fields. A prototype sensor for measuring alternating fields was made using a very simple electroscope approach. An electronic field mill sensor for dc fields was made using a fiber optic readout, so that the entire probe could be operated isolated from ground.

There are several instances in which more precise knowledge of the temperature of electrical power apparatus would be useful. This report describes a number of methods whereby the distributed temperature profile can be obtained using a fiber optic sensor.

The ability to energize electronics by means of an optical fiber has the advantage that electrical isolation is maintained at low cost. In order to accomplish this, it is necessary to convert the light energy into electrical form by means of photovoltaic cells. JPL has developed an array of PV cells in gallium arsenide specifically for this purpose. This work is described.

ACKNOWLEDGMENTS

TABLE OF CONTENTS

FIGURES

SECTION 1

INTRODUCTION

The word optic comes from the greek οπτικος, meaning eye. As a noun the word has traditionally been applied to any element of an optical system, but in particular it has been the collective noun for items such as lenses and mirrors.

One thing that such optics had in common was that they were much wider than their length. Uncounted numbers of independent rays of light can be made to pass through a small lens, for example, and a mirror reflects any light impinging upon it, regardless of the direction the light is coming from. This feature of optics, the aspect ratio, changed in the 1970s, and particularly in the 1980s, with the advent of fiber optics, optical components whose lengths are millions of times their width. In these components, the light can only be inserted into the optical element from near the axis of the fiber. Once it is coupled into the optic, light emerges from the other end almost unaltered by physical interactions between the fiber and the medium through which it passes. Modulated-light (or light which is switched on and off rapidly) can be made to pass through considerable lengths of fiber without degradation. This fact made optical fibers extremely attractive in the telecommunications industry, which has been quick to demonstrate the superiority of optical fibers as transmitters of information.

Not only are optical fibers immune to their physical and chemical environment, they are also relatively immune to the electromagnetic environment. This feature makes them of considerable interest in the electric power industry.

Since 1983, The Communications and Control for Electric Power Systems Task at the Jet Propulsion Laboratory (JPL), funded by the Department of Energy (DOE), has been investigating the application of optical fibers to power systems. A good deal of that effort has been aimed at using fiber optics as sensors in power systems.

This report is a summary of the work done at JPL in this area over the last twelve months.

1.1   POWER SYSTEM SENSORS

Electric power systems comprise some of the largest and most complicated systems in the world: They are widespread both geographically and hierarchically, that is to say they cover large areas of land and include within a given area elements of generation, transmission and distribution. They are widely interconnected and contain, from an analysis point of view, large numbers of nodes. The calculation of the state of an entire power system at any give instant is a formidable task, which even today requires several seconds of computer time on the very largest and fastest computers.

The calculations begin with measured data. In the case of a typical power system, data on many hundreds or even thousands of parameters will be collected by the Supervisory Control and Data Acquisition (SCADA) system and

relayed back to the energy control center. The measured data will typically include voltage and current at a large number of buses in the transmission system, a smaller number in the subtransmission system, and perhaps some of the distribution system parameters, as well as data concerning the status of the generators in the system. (One might note in passing that the unknown in the equation which describes the power system state is the load on the power system.)

The fact that there are so many sensed values in a power system has led to a considerable amount of interest in the development of low cost sensors based on fiber optics. Several companies, particularly in Japan, have been active in developing sensors for the primary electrical quantities (voltage and current) for ranges which are realistic in power systems, thousands of volts and thousands of amps.

At the time of this writing, fiber optic power system sensors have developed to a point where they are competitive with some of the conventional approaches, using, for example, voltage transformers and current transformers. However, they have not yet shown themselves to have a clear performance or economic advantage. This will change, nonetheless, since magnetic and capacitive sensors have been developed over many decades to a point of considerable refinement, whereas the optical techniques are just beginning to be developed.

The decision was made early on in the fiber optic sensors work of the Communications and Control Task at JPL to concentrate on developing a new measurement technique, rather than the refinement of a method of whose practicality had already been shown. The measurement of electric fields in air was chosen for the initial sensor efforts.

While the electric fields caused by power lines can be measured in the plane of the ground, their measurement outside of that plane is difficult. The development of a suitable sensor to accomplish this measurement has provided some interesting challenges.

Sensors for measuring alternating electric fields outside the ground plane had previously been demonstrated. These instruments consisted of a current measuring device placed between the electrodes of a large capacitor, measuring the displacement current between the electrodes, in such a way that the investigator could read the instrument when it was held a meter or two from him at the end of a fiberglass pole. There was typically no way to record the intensity of the electric field other than for the investigator to note the reading of the instrument.

A fairly simple modification of this principle would be to encode the data into optical form and insert it into an optical fiber which runs along the fiberglass pole. In this way the information can be read from the instrument by a data acquisition system without perturbing the electric field any more than it already is.

The measurement of direct electric fields can, in principle, be done the same way provided that the capacitor electrodes rotate (there is otherwise no displacement current in a nonalternating field).

Most of the effort of the sensor work on the Communications and Control Task during 1984-1985 has been devoted to the measurement of direct electric fields. Consequently, the largest part of this report, Section 2, is devoted to describing that work. An alternating electric field sensor was also developed during this period, and is described in Section 2.

Section 3 describes several ways of using fiber optics to measure temperature profile (temperature as a function of distance). The knowledge gained from such a measurement could be useful in both the design and the operation of a variety of electrical apparatus, such as cables and transformers.

The development of optical diodes for the transfer of small amounts of electric power over fibers is described in Section 4. Diodes such as those described could be used to provide power for electronics used in measurements in parts of the power system that are relatively inaccessible, such as in a high-voltage bus. The diodes being developed at JPL are made of gallium arsenide, a semiconductor capable of higher efficiency conversion than the more usual silicon when made into the small sizes required for this kind of application.

SECTION 2
ELECTRIC FIELD MEASUREMENT

2.1   INTRODUCTION

The magnitude of the electric field under a transmission line, or in a substation, is of considerable interest because of possible environmental impact. In the absence of ion current the field may be calculated if the geometry is fairly simple, but for even a moderately complex geometry the calculation can become difficult and expensive to carry out. Under a high voltage dc transmission line in corona, measurement is the only practical way to determine the field.

Existing electric field sensors typically have conductive electrodes and some form of cabling connecting them to the measurement electronics. This arrangement can cause considerable distortion of the unknown field if the measurement is to be made above the ground plane. In one implementation for ac measurements (Deno and Zaffanella, 1975) the sensor is self-contained, and furnished with a scale large enough that an operator a meter or two away can read it visually. The device is calibrated in a uniform field in a large test chamber. However, the probe is relatively large, and it distorts the field nearby, introducing an error if the field is non-uniform (as it would be near another conductor.) There is clearly some advantage to a small, all-dielectric sensor.

In other approaches, Feser and Pfaff (1984) described a small (4.0 cm diameter) probe connected to measurement electronics by fiber optics for electrical isolation. Earlier experiments along the same line were reported by Wilhelmy (1972). Misakian and his co-workers (1978) described an even smaller spherical probe (1.2 cm diameter), although it was connected to its electronics with copper wires which had to be placed along an equipotential surface of the measured field.

These instruments were all intended for measurement of ac or transient fields. However, the work of Feser and Pfaff, and especially Misakian, has demonstrated that small probe dimensions are needed for field measurements within a few centimeters of irregularly shaped, conductive objects.

For the measurement of the field under a direct-current line, the induced charge on the probe must be modulated in order to make it measureable. Previously reported instruments intended for dc field measurement have been designed with rotating or vibrating electrodes to modulate periodically the acquired charge. The resulting device is then known as a field mill or a vibrating plate electrometer, respectively. Comparative tests of a number of these instruments under a dc line have been reported in the literature (Comber, Kotter and McKnight, 1983). All of the instruments described operate with part of the system grounded, and must be mounted in the ground plane. Examples of field mill designs are shown in Figure 2-1.

This report describes the work done at JPL on the design of an all-dielectric ac field meter, and an isolated-probe dc field sensor. Both sensors use fiber optics, but in quite different ways.

FIXED, GROUNDED
SHIELD ELECTRODE

ROTATING SENSOR
ELECTRODE

GROUNDED PLATE

SIGNAL OUTPUT

ISOLATED
CONDUCTIVE SHAFT

BRUSH

a) WITH ROTATING SENSOR ELECTRODE

ROTATING, GROUNDED
SHIELD ELECTRODE

FIXED SENSOR
ELECTRODE

GROUNDED PLATE

SIGNAL OUTPUT

GROUNDED
SHAFT
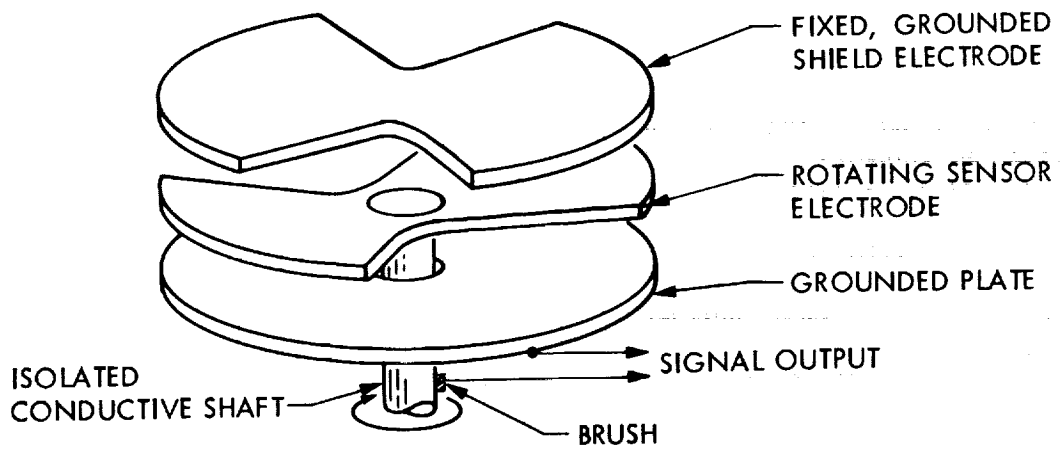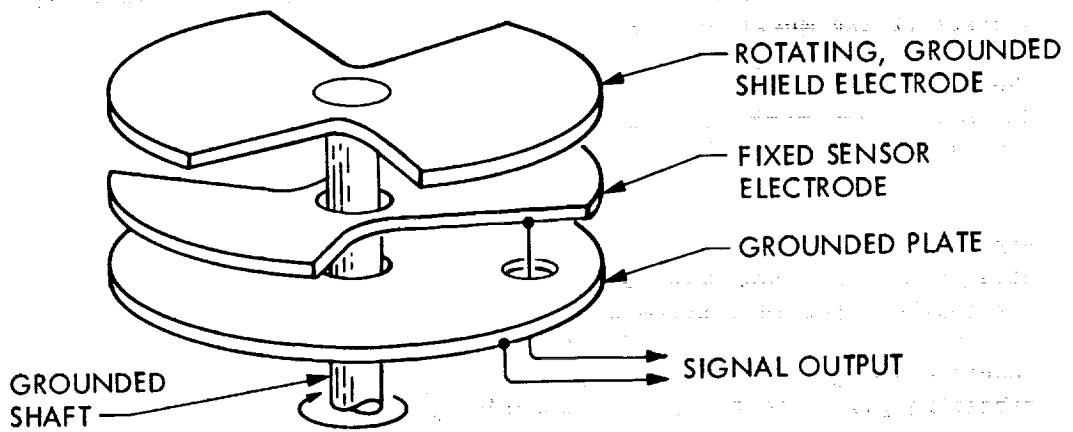
b) WITH FIXED SENSOR ELECTRODE

Figure 2-1. Examples of Field Mill Designs

2.2 AC FIELD MEASUREMENT

A compact electroscope for measurement of ac fields was investigated. A number of feasibility models were fabricated, and test data were obtained. The basic principle involved was to detect a field-induced force on a quartz fiber or fibers by measuring their flexure optically. The fibers used in the electroscope were optical fibers with core and cladding, which could readily be connected to a monitoring instrument via cables containing similar fibers. The basic idea was described in an earlier report (Kirkham, Johnston, Lutes, Daud, and Hyland, 1984).

There are a number of attributes, both good and bad, that distinguish the quartz fiber electroscope from other devices for field measurement. On the good side, the device could be made very small: a package on the order of 5 mm in diameter and 20 mm long should be quite practicable. No power is required at the device, it is completely passive. It is possible, as will be described later, to build the sensor of dielectric materials only. No conductors need be present. This is attractive in applications involving measurement of very high fields where corona effects or air breakdown at structural discontinuities must be guarded against.

On the negative side, the device is inherently non-linear, and is sensitive to acceleration. The latter point, acceleration or g-sensitivity, is strongly dependent on the electroscope geometry. A single cantilevered fiber used as the sensitive element is clearly g-sensitive. Experimental tests showed that 1g could produce an output corresponding to a significant fraction of the full scale deflection. On the other hand, it is possible to compensate for acceleration-induced response by building a two-fiber electroscope such that both fibers deflect together, eliminating significant relative motion under g-forces, but deflect oppositely due to electric field-induced forces. Compensation of g-forces or vibration effects were not investigated experimentally. A final factor that is not necessarily emphasized is that the device responds inherently to E^2, which makes it blind to the sign of a field. It will measure fields in either direction along its sensitive direction, consistent with its being considered an ac sensor. In fact, the device can measure high frequency or RF fields as well as those at power frequency, which may suggest other applications.

In order to facilitate building of test models of the electroscope by a skilled technician, but one untrained in techniques for making fused silica, a design was worked out which was based on building the device up from microscope slides and glass spacers cut from microscope slides. UV curing cement was used for assembly.

The configuration is illustrated in Figure 2-2. A conductive coating was placed on the fiber itself and on a very small area of the mounting slide immediately under the fiber. The sensitive field direction is perpendicular to the microscope slide base.

TWO FIBER CABLE

SPACER

MOVING
METALLIZED FIBER

SPACER

GLASS SUBSTRATE

METALLIZED TRACK

FIXED FIBER
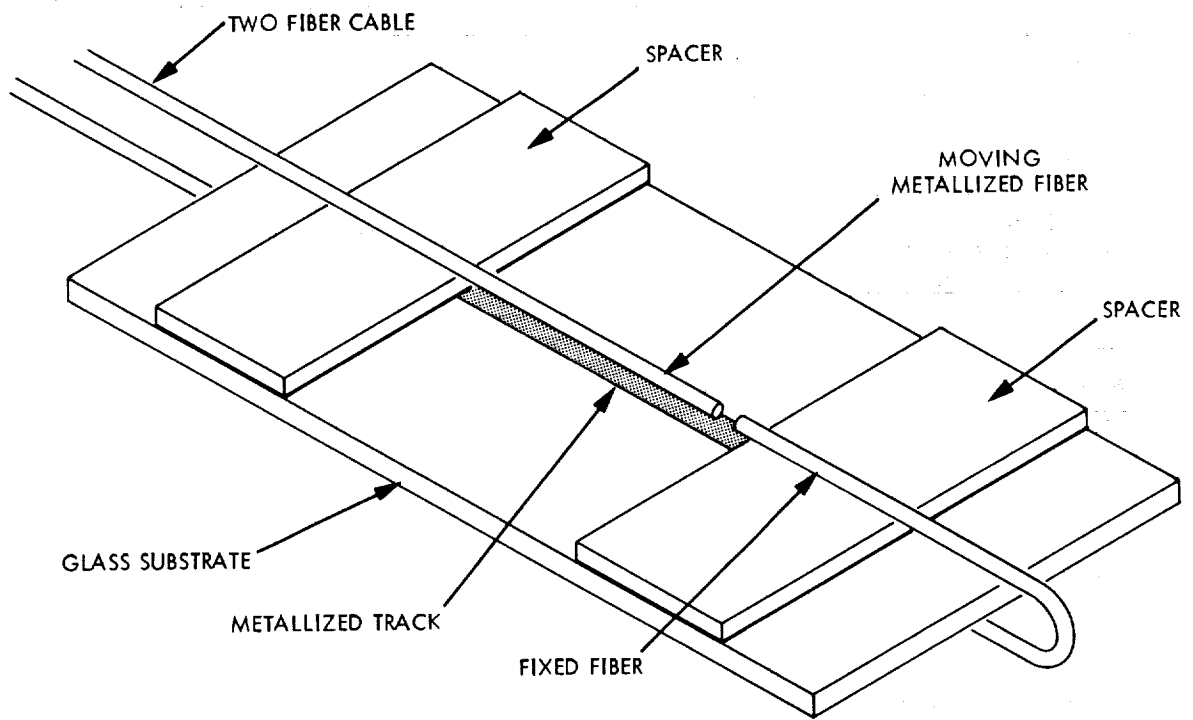
Figure 2-2. Laboratory Model of Fused Silica Fiber
Electroscope with Metallized Fiber

2-4

The photograph shown in Figure 2-3 shows the feasibility model, with the sensor mounted in a lucite tube together with the accessing fiber optic cable and a readout box. No effort was made to miniaturize this model. A representative curve of output versus applied field is shown in Figure 2-4.

An alternative design is shown in Figure 2-5. In this configuration, the sensing fiber is placed at the end of a gap or slot between two field-shaping pieces of dielectric. The field-induced force arises as a result of locating the sensing fiber in a strong field gradient created by the dielectric slot. No metal or other conductor is used in the device. Several test models of this all-dielectric configuration were built, and they all functioned well.

These sensors are best suited to measurement of large fields, 100 kV/m or more, but they can, with difficulty, be scaled for lower fields, down to perhaps 10 kV/m.

A number of applications for these unique sensors were discussed with other workers in the power industry. Examples are briefly described below.

(1) It should be possible to monitor the state of very large circuit breakers using variations in field near the gap. This field is dependent on the position of the contacts. It would not be possible to directly measure contact position with any conventional devices because of the potentials involved.

(2) A 'hot-stick' with a very simple and robust sensor encapsulated in it would be a valuable safety tool for service personnel. The sensor could detect a live conductor on approach and trigger an alarm signal.

(3) A simple dielectric device that could be manipulated in proximity to a long insulator string could be used to detect a shorted module in the string. Multiple failures of this type could result in a failure of the entire string. Failure ('puncture') detection of this kind could improve insulator string performance.

A simple test of this idea was conducted at General Electric's High Voltage Transmission Research Facility (HVTRF) in Pittsfield, Massachusetts during a visit there last year by JPL personnel. Detection of a deliberately shorted element in a short insulator was readily done.
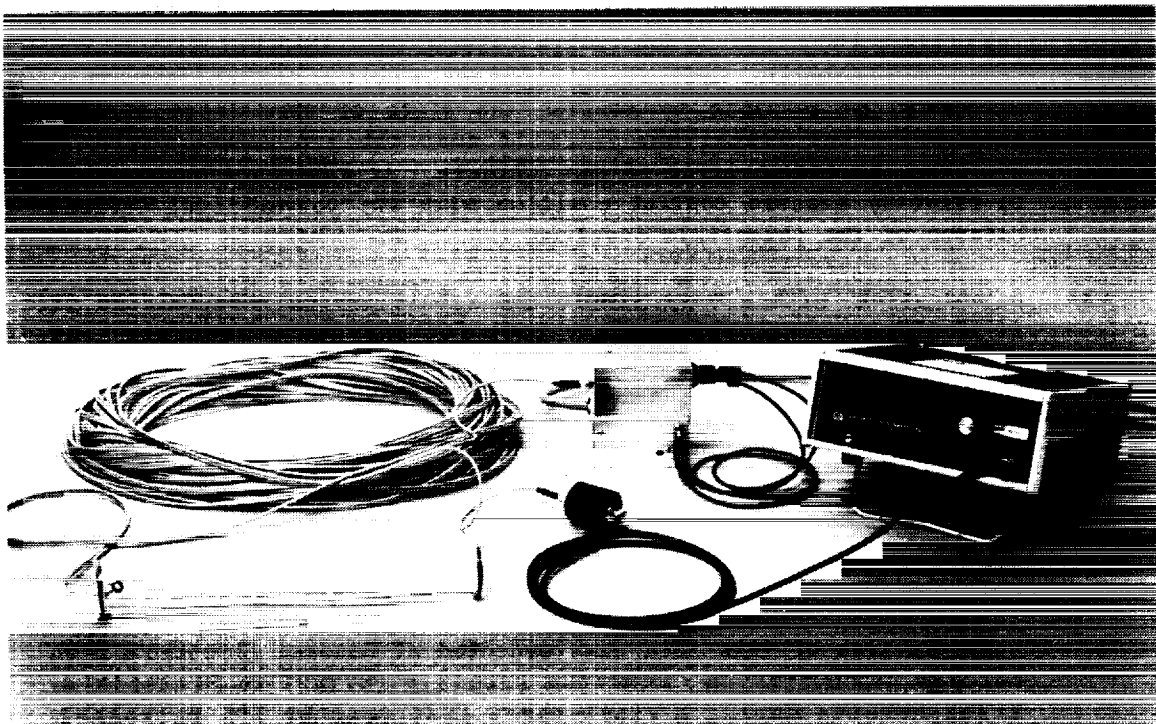
Figure 2-3. Photograph of the Fiber Electroscope as Built
(The microscope slide base is mounted on a larger
dielectric mounting board)
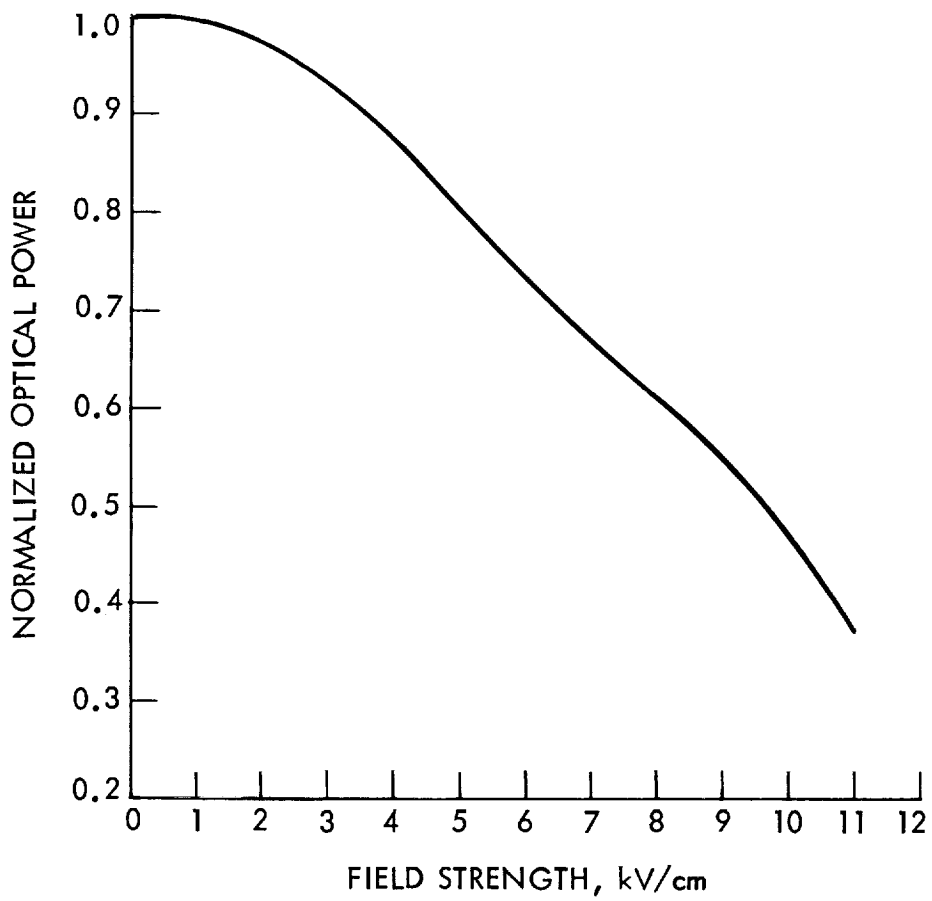
Figure 2-4. Input-Output Curve for an All-Dielectric Test Model
of the Fiber Electroscope

SPACER

DIELECTRIC ELECTRODE

SPACER

GLASS SUBSTRATE

DIELECTRIC ELECTRODE
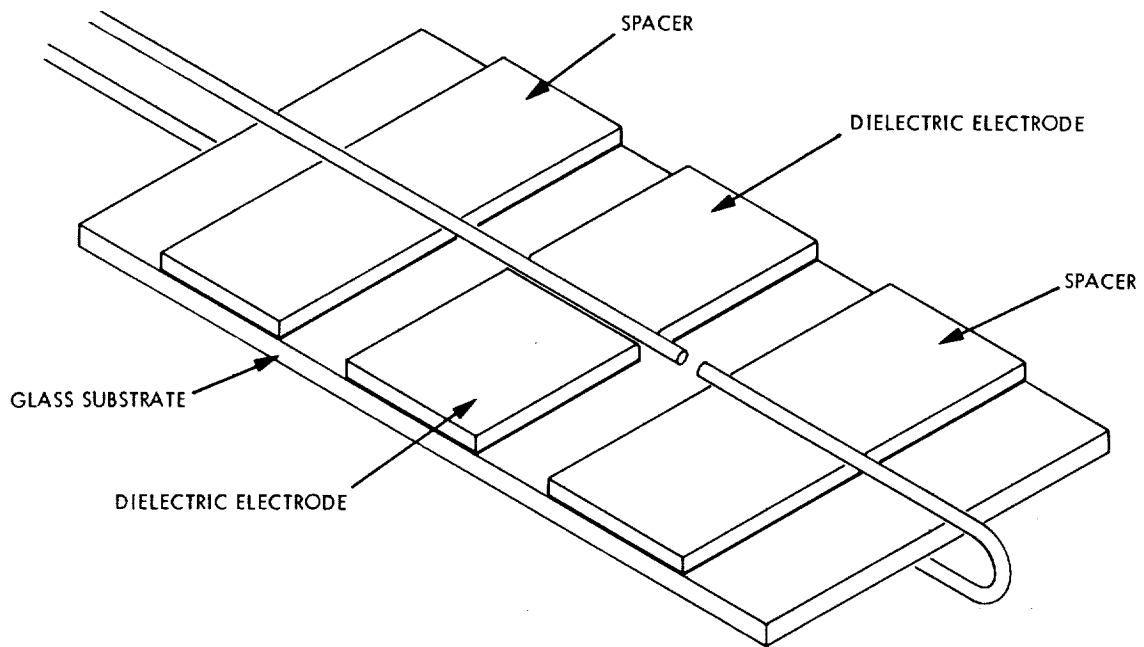
Figure 2-5. An All-Dielectric Configuration of the Fiber Electroscope Sensor (No Metal or Conductive Coatings are used)

2.3   DC FIELD MEASUREMENT

In contrast to the situation under an ac transmission line, ion current is a characteristic part of the environment under a High Voltage Direct Current (HVDC) line.

The ions of interest are produced by corona processes at the conductor surface, and accelerated away from the conductor by the electric field. The density of the atmosphere is such that the subsequent motion of the ions is dominated by collisions with atmospheric molecules, and an ion of given size and charge will acquire an effective velocity determined only by the field. Such motion is usually described in terms of ion mobility. Ions may be thought of as drifting along field lines, at a velocity given by the product of the field and the mobility. Any ion current present will flow into a grounded instrument, or will deposit charge an electrically isolated instrument. As a result, the instrument must be capable of distinguishing between field-induced charge and ion current. With field mills mounted in the ground plane, the two modulated current components are in phase quadrature, and can be separated by phase sensitive detection (Maruvada, Dallaire, and Pedneault, 1983). However, the same technique, when applied to a grounded rotating cylinder field mill (Maruvada et al., 1983) required two sensors rotating at different speeds to separate the ion current component from the field-induced output. The device in question had two significant drawbacks. It was large (over a meter in length), and it was grounded.

The sensor described in this report is of the rotating cylindrical field mill type, but it is quite small, less than 20 cm long and 10 cm in diameter. Further, it utilizes a fiber-optic readout to isolate the probe electrically from ground. Therefore, no ion current can flow to the probe in the steady state. Instead, it will acquire a charge sufficient to prevent additional ion current from flowing to it. The effects of self-charging due to ion current are discussed briefly in the following section.

As noted above, instruments capable of measuring electric field at space potential have been available for some time for ac use. Similar dc instruments suitable for use in the field have been described in the literature, but are not routinely made. Free space dc measurements have been made in the laboratory using a Pockels crystal (Hikada and Fujita, 1982). The availability of measurements of dc electric field at space potential will make possible better evaluation of the field effects due to dc lines, and put dc measurements on an equal footing with ac measurements.

2.3.1   Theoretical Background

The principles involved in the design of our electric field sensor can be understood with respect to Figure 2-6. The external electric field is determined by measurement of the displacement current between two shorted, semi-cylindrical rotating electrodes. In the figure, the radius of the cylindrical electrodes is r, and the split between the two halves is at angle β with the x axis. A uniform field E_0 is directed along z and the axis of the cylinder is along y. Under these conditions, the surface charge density σ
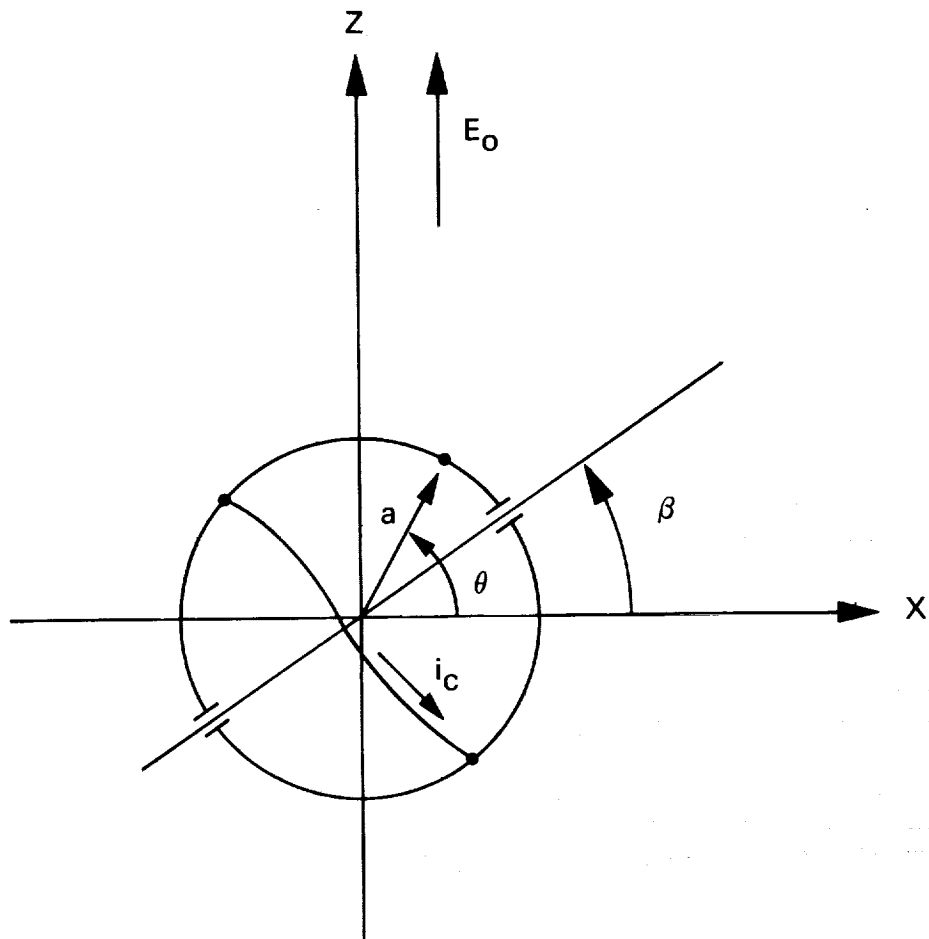
Figure 2-6. Geometry of Split-Cylinder Sensor Probe

on the cylinder at azimuthal position θ is easily derived, and is given by

$$\sigma = 2 \; \varepsilon_o \; E_o \; \sin \theta \qquad (2-1)$$

The total charge on the cylinder is assumed to be zero, which means that its potential is set at the value existing at the location of its axis before it is introduced into the field.

By integrating over one half of the cylinder, the total charge on one of the electrodes can be evaluated as a function of the electrode orientation angle $\beta = \omega t$. Differentiation with respect to time yields the current i_c in a wire connecting the two half cylinders of length 1:

$$i_c = 4 \; \varepsilon_o \; E_o \; 1 \; r \; \omega \; \sin \omega t \qquad (2-2)$$

Therefore, if the rotating sensor is placed in a uniform field far from any conducting surface, its output is sinusoidal, with amplitude proportional to the field E_o. The current i_c is measured electronically and telemetered as a measure of the field E_o.

A similar analysis, applied to a split sphere rotating about an axis through the split, yielded a short circuit current i_s of

$$i_s = 3\pi \; \varepsilon_o \; E_o \; r^2 \omega \; \cos \omega t \qquad (2-3)$$

This result is different by a constant factor from the cylindrical case ($i_s/i_c \sim 1.2$ for $1 = 2r$), indicating that the finite length of the actual sensor probe does not affect the foregoing argument significantly.

If the sensor is subjected to an ion drift current, it will acquire a charge. The effect of this charge can be estimated by superposing the field from a charged conducting cylinder and the previously discussed uncharged cylinder immersed in a uniform field.

The field component resulting from the charged cylinder is independent of θ in the absence of nearby conductors, and, therefore, can make no contribution to the measured field-induced current i_c. Consequently, the sensor will not respond to a steady-state self-charge if it is far from any conducting surfaces.

The error introduced by self-charging when the sensor is near a conducting surface can be estimated using the following argument. Assume that the sensor is located in a semi-infinite region of uniform field bounded by a ground plane, with the sensor axis at distance d from the ground plane, and that an ion drift current flows toward the ground plane. The sensor, assumed to be an infinite cylinder, will intercept a small portion of the ion current, acquiring a charge Q per unit length.

Under these conditions, the field in the neighborhood of the sensor can be specified approximately as the superposition of three components, the uniform field (as perturbed by the presence of the uncharged conducting sensor cylinder), the field of a line charge Q on the sensor axis, and the field of an image line charge $-Q$ reflected in the ground plane at a distance 2d from the sensor axis. Additional secondary images resulting from the presence of the conducting cylinder in the field of the image $-Q$ are neglected.

As we have seen, the field of the line charge on the sensor axis is not detected by the sensor. However, the field component from the image charge would be detected, and gives an approximate estimate of the error if the distance d is large.

In order to estimate the magnitude of the line charge, Q, note that ion current flow into the sensor will stop when the field component at its surface due to the self charge Q exactly cancels the field due to the external uniform field at points on the cylinder opposite the ground plane ($\theta = \pi/2$ in Figure 2-6). When this is true, there no longer is a field component at any point on the surface of the cylinder causing an ion drift toward the cylinder. Since the field on the top surface of the cylinder at $\theta = \pi/2$ in a uniform field E_0 is $2 E_0$, the condition for charge collection to stop is

$$2 E_0 = \frac{Q}{2\pi\varepsilon_0 r} \tag{2-4}$$

It follows that the magnitude of the field E_i at the axis of the sensor due to the image charge is

$$E_i = \frac{Q}{2\pi\varepsilon_0 (2d)} \tag{2-5}$$

and the error caused by self-charging obtained by combining equations 4 and 5 is

$$\frac{E_i}{E_0} \sim \frac{r}{d} \qquad \text{for } r/d \ll 1 \tag{2-6}$$

Again, an analogous estimate was carried out assuming a spherical sensor instead of a long cylinder, with the result:

$$\frac{E_i}{E_0} \sim \frac{3}{4} \frac{r^2}{d^2} \qquad \text{for } r/d \ll 1 \tag{2-7}$$

These two estimates set limits on the error expected for the actual sensor geometry. Note that the result does not depend on the ion current density.

It assumes only that the sensor charges fully, satisfying the surface field condition (Equation 2-4). If full charging does not occur, the error will be proportionately less.

The above expressions are not accurate if r is not much smaller than d. Although exact analytical expressions in terms of a series can be derived using the image method, the slow convergence of the resultant series prompted us to find a numerical means of solving this problem. Using the finite-element technique, a numerical method was used to find the potential $V(x,y)$ everywhere within a given enclosed region, provided that the potentials on the bounding surfaces are known. This approach was applied to the problem of an infinite cylinder near a ground plane.

Because of symmetry, only half of the structure needs to be included. This region was divided into 260 x 130 equally spaced subregions. Given V_1, V_2 and V_3 on the bounding surfaces, respectively, the ground plane, the cylinder and a plane surface parallel to the ground plane but far enough from the cylinder not to influence the results, the potential at each grid point was calculated. Knowing the voltage everywhere, the electric field can readily be calculated, and the resultant charge on the surface of the cylinder is proportional to the normal component of the electric field E_r there. Summing over all the charges on the upper half of the cylinder yields the total charge Q_u and summing over all the charges on the lower half yields Q_1. The quantity $Q_a = (Q_u - Q_1)/2$ is taken as a measure of the sensor output, since the charge distribution is not symmetrical when the sensor is near the ground plane.

The fractional change in Q_a, $\Delta Q_a/Q_{ao} = (Q_a - Q_{ao})/Q_{ao}$ is plotted in Figure 2-7 as a function of d/r. Q_{ao} is the calculated value of Q_a calculated for $d/r \gg 1$, that is, with the sensor in free space.

The quantities $\Delta Q_a/Q_{ao}$ and E_i/E_o (Equations 2-6 and 2-7) are directly comparable, and are a measure of the change in sensor output due to the presence of the ground plane. The condition for charge equilibrium in the presence of ion current (Equation 2-4), was imposed in calculating $\Delta Q_a/Q_{ao}$.

It can be seen that a significant change in sensor output can be produced by a nearby conductor. However, these results indicate that if the sensor is kept at a distance greater than approximately five times its own radius from the nearest surface, the error will be less than 10%. In addition, estimates made using a two dimensional cylindrical model are upper limits on the perturbation that would be seen by a sensor probe of finite length. If the sensor is not much closer to a surface than its own length, then the perturbations will be smaller than the two dimensional model predicts.

The response of similar probes in nonuniform fields has been treated by other authors (Wilhelmy, 1972; Misakian et al, 1978). Their results show that the sensor response indicates the field at the location of the center of the probe before the probe is introduced. Errors of the order of 1% or less were predicted when the undisturbed field varies by tens of percent over the volume of the probe. It can be concluded that the dominant error source is image fields resulting from self-charging when near a conducting surface.
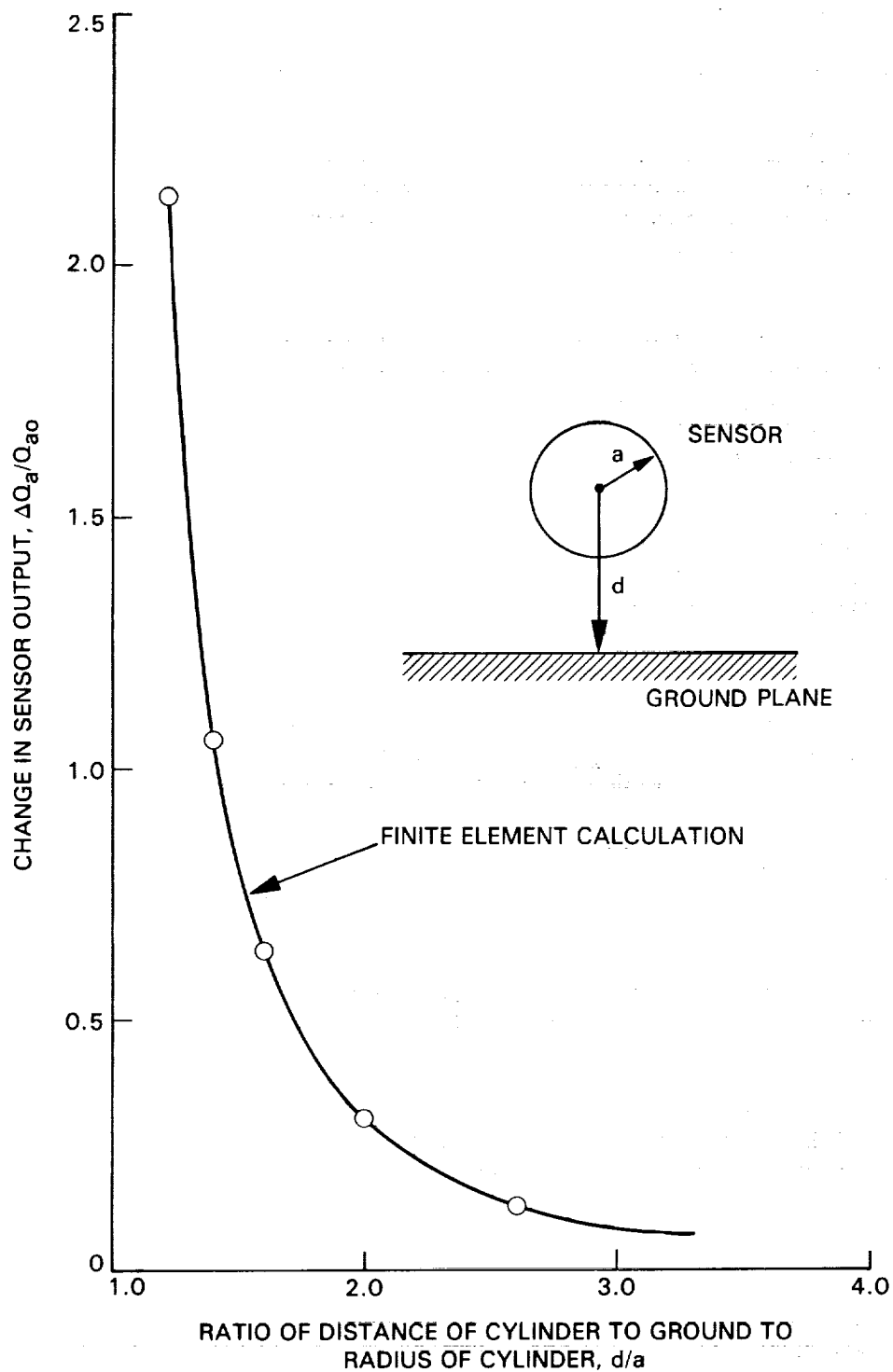
Figure 2-7. Fractional Change in Sensor Output Induced by a
Nearby Conducting Surface for Full Ion Current
Charging

2.3.2   Sensor Design

The overall instrument consists of two parts: (1) the sensor probe, which is self-contained and isolated from ground, and (2) a set of readout electronics, providing an output suitable for use by a data acquisition system. The two parts are connected by a conventional 100 micrometer diameter core multimode fiber optic cable. The overall cable diameter including strength members is about 3 mm.

The unconventional aspects of the instrument are located in the sensor probe, which will be briefly described. A stationary tube supports the rotating sensing head, and carries a small battery powered dc motor to drive the surrounding rotating element. The rotating element contains an electronics package, powered by separate watch-type batteries, which measures both the displacement current between the two electrodes and the position of the rotating part of the sensor with respect to the stationary part. This information is encoded in terms of pulse repetition frequency and used to drive an LED transmitter.

A rotary optical coupler transfers information from the rotating electronics into a non-rotating fiber cable termination mounted on the axis of the supporting tube. No use is made of slip rings or rotary transformers.

The entire sensor, including its drive motor and battery, the rotating electronics and its battery, and the fiber-optic coupler, is housed inside the split cylindrical sensing electrode pair, as shown in Figure 2-8. No particular effort was made, for this prototype, to produce a miniature instrument. The sensor is about 8 cm in diameter and 20 cm long. It is intended, in subsequent phases of development, to reduce the sensor size by about an order of magnitude in its linear dimensions. Such a sensor should enable free-body field measurements to be made of fields which vary significantly over distances of only a few centimeters, providing data on the magnitude of electric fields after they have been perturbed by the presence of an animal or a man.

The block diagram shown in Figure 2-9 shows the principle of operation. The externally mounted cylindrical electrodes are connected to an operational amplifier configured in a charge measurement (integrating) mode. When the sensor rotates in a dc field, a current is induced between the two half-cylinders which is proportional to the rotational frequency as well as the field, as shown in Equation 2-2. This frequency-dependence is removed by the capacitive feedback element in the amplifier, resulting in a periodic output signal which is independent of rotational speed. This signal, in turn, modulates a voltage-controlled oscillator (VCO). Position-reference information is then combined with the VCO output in the encoding logic block, which creates a coded train of short pulses for optical transmission. The optical link transfers the pulse train to the readout electronics where the field amplitude and position reference signals are reconstructed and measured.

2-15
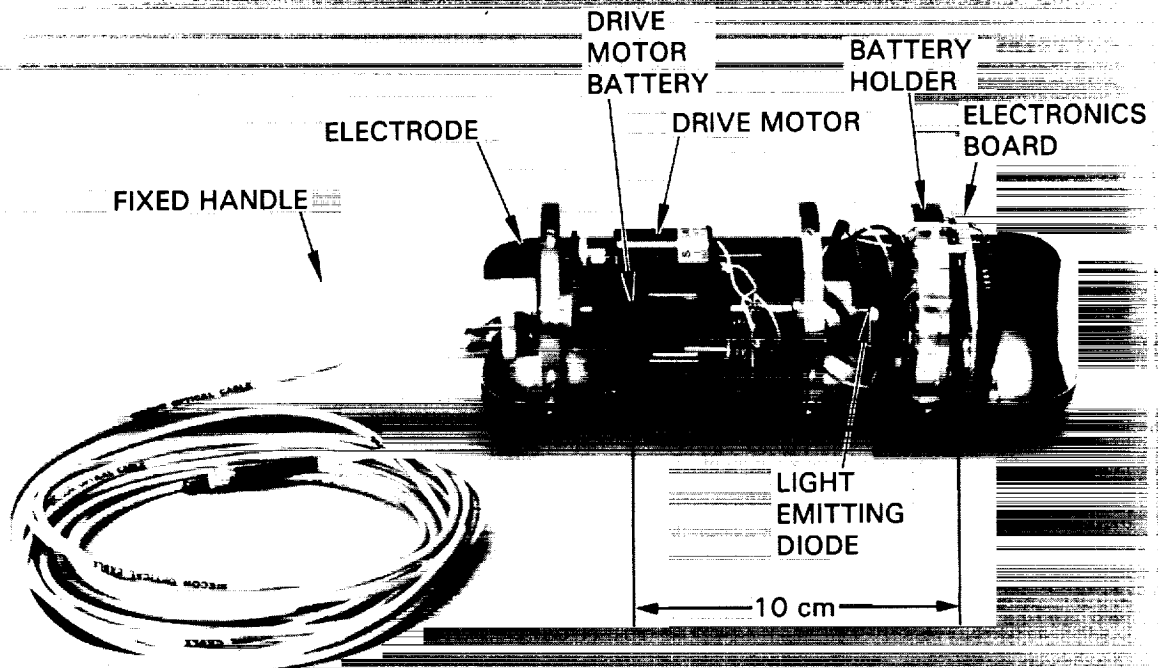
Figure 2-8. Photograph of the Prototype Sensor with One-Half
Cylindrical Shell Removed to Show Internal Parts

SENSOR
PLATES

E   i

INTEGRATING
AMPLIFIER

V

VOLTAGE
CONTROLLED
OSCILLATOR

f

REFERENCE
POSITION
SENSOR

⎍

ENCODING
LOGIC

‖‖‖

FIBER OPTIC CABLE

LED WITH
ROTATING
COUPLING

REFERENCE
POSITION
DECODER

RECEIVER
MODULE

SIGNAL
DEMODULATOR

OSCILLOSCOPE
OR LOCK-IN
AMPLIFIER

DVM
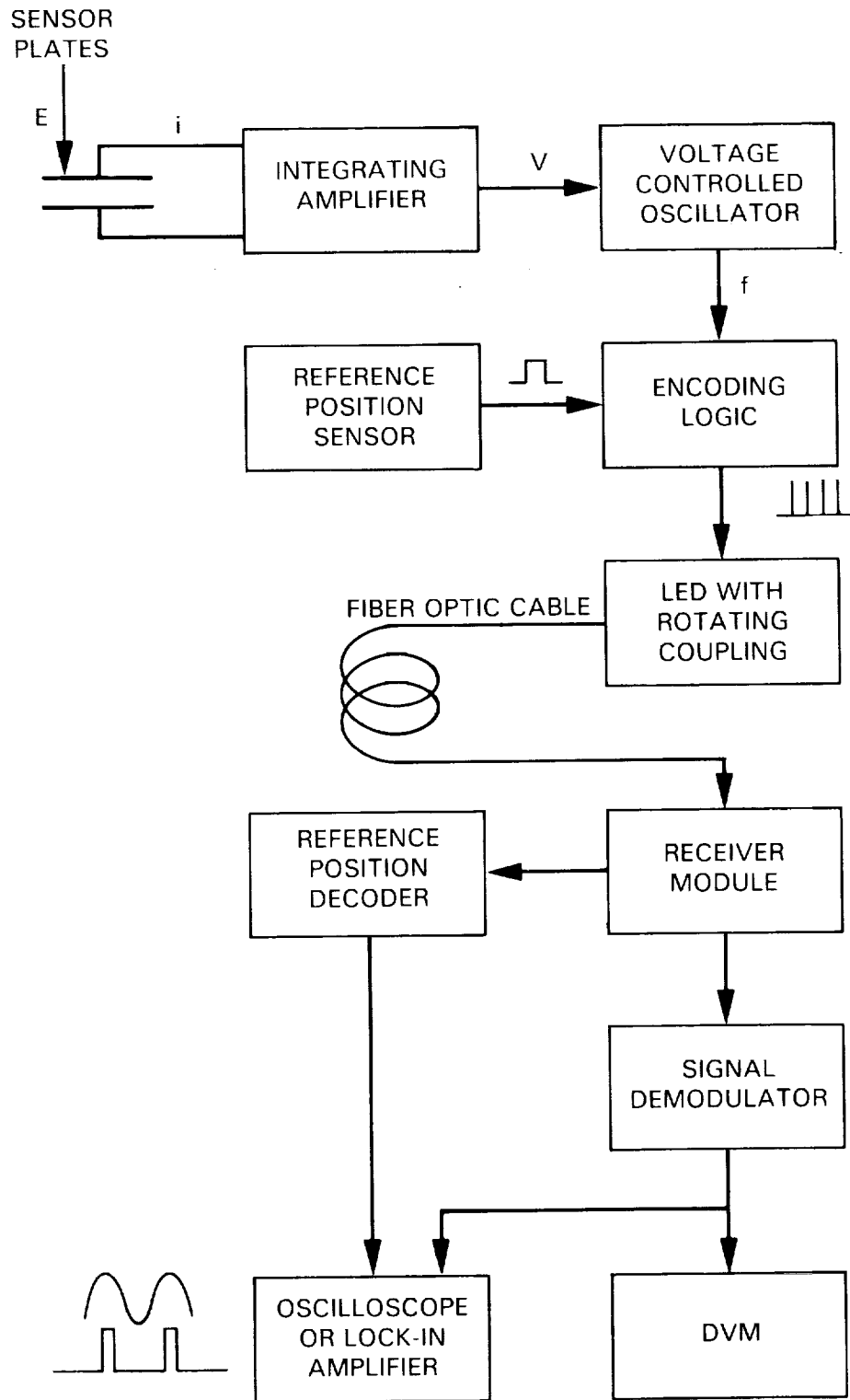
Figure 2-9. Functional Block Diagram of the Sensor Electronics

2-17

2.3.3 Position-Reference Encoding

The position-reference signal is needed in order to obtain the angle of the electric field vector as well as its magnitude. In this design, a phototransistor on the rotating part of the sensor passes in front of a stationary light-emitting diode (LED) once every revolution, sending a signal to the encoder to mark the reference position. The optical transmitter normally generates a short pulse (0.25 μs) at each positive transition of the VCO output. When the signal from the position-reference phototransistor is received, the next optical pulse is replaced by two pulses in close succession. The addition of the reference pulses to the data-pulse train does not disturb the amplitude signal, and gives an average angle resolution of 1.5 degrees (at 2400 rpm).

2.3.4 The Optical Link

The optical link consists of an LED transmitter, an appropriate length of fiber-optic cable, and a receiver module with a built-in amplifier. A standard fiber-optic connector was modified to provide the rotary coupling between the sensor and the cable. The encoding format, a very low duty-cycle pulse frequency modulation, was chosen to conserve battery power, with the object of increasing the duration of operation of the instrument.

A schematic of the sensor head and the receiver system is shown in Figure 2-10. Figure 2-11 shows the sinusoidal output, as seen at the demodulator output of the receiver for a dc field at the sensor head of 30 kV/m.

2.3.5 Laboratory Evaluation

Laboratory evaluation of the sensor gave the following results:

(1) Direct fields ranging from 70 V/m to 50 kV/m, a dynamic range of roughly 10^3, were measured using an ac voltmeter to read the output voltage. Within the above range the sensor was linear to within 2%.

(2) The measured ac output voltage was independent of frequency (within 1%) over a range corresponding to sensor speeds between 600 and 4200 rpm, as shown in Figure 2-12. With a new 9 V battery, the sensor rotates at approximately 2400 rpm.

(3) The current drain of the rotating circuitry was less than 1.4 mA at 6 V. This was measured with the encoder driving the LED with 40 mA pulses at a center frequency of 10 kHz, giving an optical power margin of 6 dB. The LED accounted for less than 10% of the total current drain. The pulse-coded fiber optic data readout does not dominate the power requirement of the rotating circuitry. The present power drain is approximately 8 mW, but an optimized design could reduce it significantly.

Taken together, the results of the laboratory tests show that the sensor is capable of measuring the field-induced charge on its electrodes within ~2%
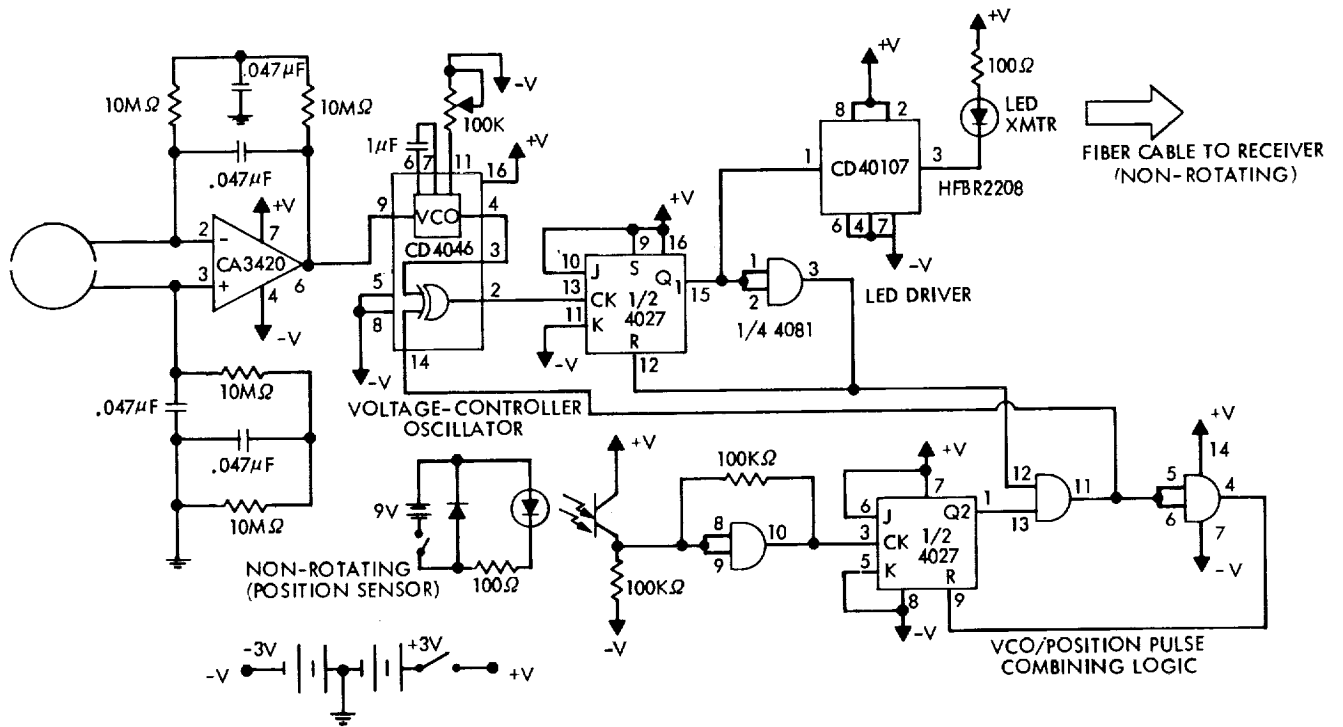
Figure 2-10a. Schematic of DC Field Sensor Probe
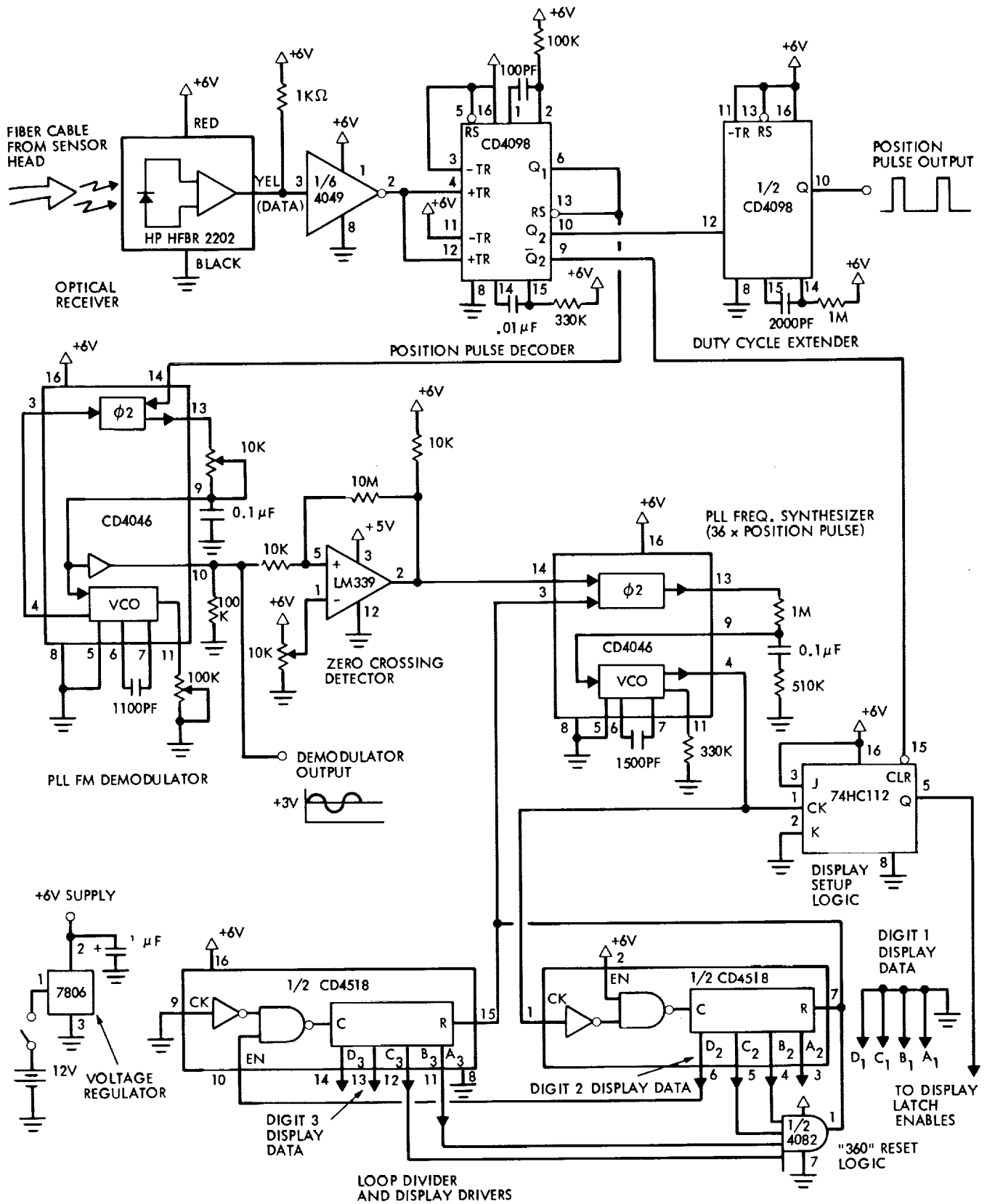
Figure 2-10b. Schematic of DC Field Sensor Receiver

2-20
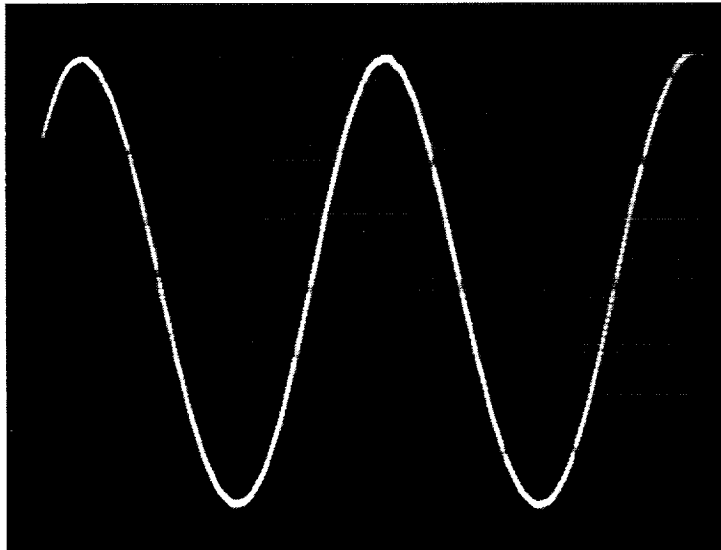
Figure 2-11. Typical AC Output as Seen at the Receiver
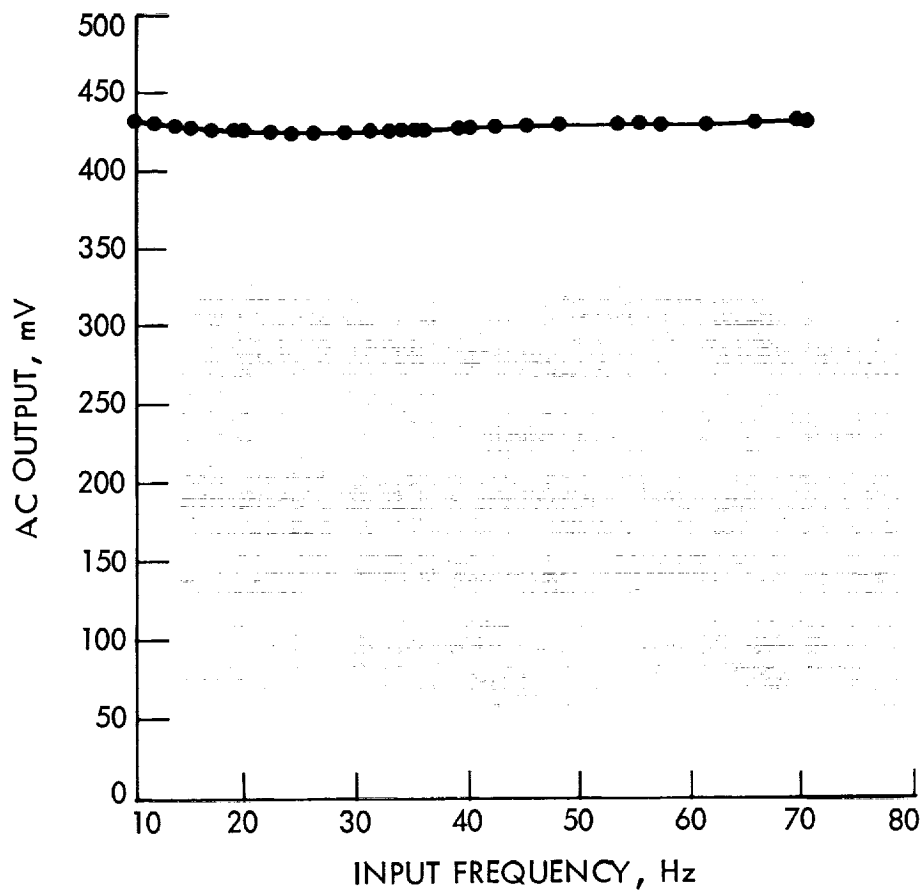
Figure 2-12. Output of Sensor at Rotational Frequencies Corresponding to Speeds between 600 and 4200 rpm

2.3.6   FIELD TESTS

The prototype sensor was taken to General Electric's High Voltage Transmission Research Facility (HVTRF) near Pittsfield, Massachusetts, for evaluation in a more realistic environment using facilities described in earlier reports (Comber and Johnson, 1982; Comber et al., 1983). Three types of measurements were undertaken: (1) sensor response in a large test chamber used for field calibration, (2) a field survey under a unipolar dc transmission line, and (3) demonstrations of the kind of measurements possible only with an isolated sensor: measurements of the field above the permanent equipment at the measurement location, and around a person standing directly under the line. The results of these initial measurements are given in the following paragraphs.

As was pointed out earlier, the environment around a full-scale transmission line is characterized by space-charge and ion current, as well as the electric field. The space-charge significantly modifies the electric field, and the magnitude of the space-charge field varies with time and weather conditions. Of more concern to free space field sensing, the ion current will deposit charge on any electrically isolated object, including the sensor and its supporting dielectric pole. The effect of the collected charge on the field measurement must be understood in order to make dependable and accurate field measurements. As will be seen, the data obtained in the test cage do show a response which is thought to be due to self-charging, although its magnitude is not large.

The sensor response was determined in a planar test cage which had a 92 cm spacing between the ground plane and the energized electrode. The cage was cylindrical, approximately 3 m in diameter (Comber et al., 1983) and had two peripheral grading rings to minimize the effect of fringing. The sensor was placed on the axis of the cage approximately 30 cm above the ground plane. For this measurement, and for those described below, the sensor was supported by a fiberglass pole 2.5 cm in diameter and 3 m in length. The pole was oriented along the projected axis of the rotating sensor, although there was a small (~ 2 cm) offset between the axis of the pole and the axis of the sensor. The surface resistivity of the pole was not known.

The calibration curve obtained in the cage is shown in Figure 2-13. The applied field, shown on the abscissa, is based on measurement of voltage and electrode spacing. The plot represents one excursion from zero field to maximum and return. The indication from a separate field probe (Monroe Electronics) located in the ground plane of the test cage is consistent with the small hysteresis loop seen in Figure 2-13 and the droop of the curve below a linear response being due to self-charging of the sensor probe, or the pole used to support it. The magnitude of the perturbation averaged 3%. No attempt was made to monitor field direction in the test cage.

The second set of data, shown in Figure 2-14, was obtained in order to illustrate the type of field-mapping above the ground plane which is possible only with an electrically isolated probe.
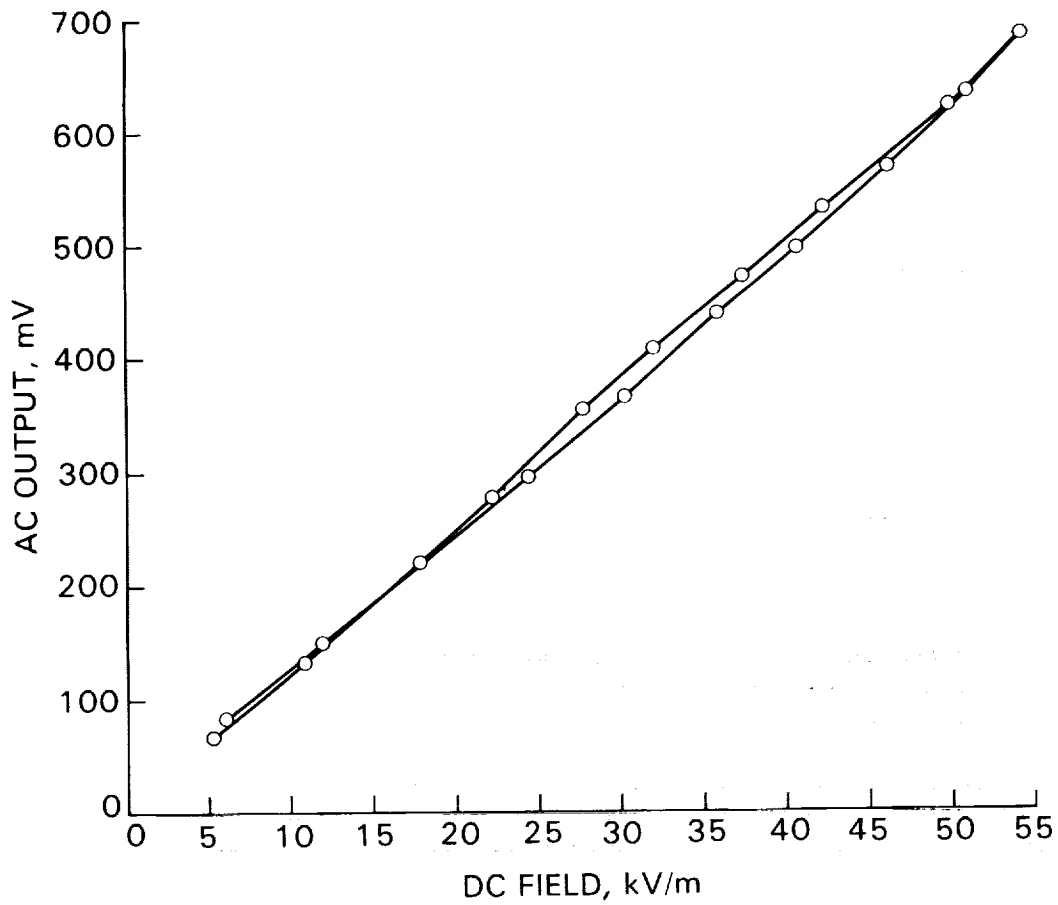
Figure 2-13. Calibration Curve Obtained in HVTRF Test Cage

Field measurements were made around a person while he was standing directly under the conductor of the short test line at the HVTRF. The fiber glass pole was counterbalanced (for convenience) and the field readings were noted on a large Polaroid photograph which included the test subject. The sensor is shown in Figure 2-15, held by Dr. Gary Johnson of HVTRF. The test subject is Björn Eng of JPL. The conductor was charged to -200 kV dc for this experiment, which yielded an average field at ground level directly under the conductor of 7.7 kV/m, and an ion current density varying between 0.5 and 5.0 nA/m^2 as measured by the HVTRF data system located in the ground plane. The prototype sensor measured 6.2 kV/m at 1/2 m above the ground surface without the human subject being there.

In the figure, the length of each arrow indicates the magnitude of the field as measured at the location of the arrowhead. The sensor, attached to the 3 m fiberglass pole, was held stationary for a short period of time (~ 10 sec) at each position indicated in the figure. One of the investigators recorded the output of the sensor, while another noted the location of the sensor. To facilitate estimating the sensor position, a large-format instant photograph was made, and a grid was drawn on it. The position of the sensor probe was noted in terms of grid coordinates by reference to the photograph. The uncertainty of the position was roughly $\pm$ 5 cm. Figure 2-14 was later produced from this photograph, by combining the appropriate position, amplitude, and direction information. Field direction was measured visually on an oscilloscope (by a third investigator), using the phase of the angular position reference signal transmitted from the rotating sensor head. The direction measured without the person being present was assumed to be vertical and used to calibrate the position output. The accuracy of field direction was roughly $\pm$ 20°. Instrumentation for precise, direct readout of field angle has subsequently been completed. The observed field at a location 20 cm above the head was 20.8 kV/m, 3.4 times the undisturbed field at ground level.

For comparison to the measured values, field intensification over a conducting prolate ellipsoid, placed with its axis perpendicular to a conducting ground plane and its center on the ground plane, was calculated as a function of the aspect ratio of the ellipsoid and the height above the ellipsoid surface. On the top surface of the ellipsoid, corresponding to the top of the head, a field intensification by a factor of 23 was obtained for an aspect ratio (semi-major axis/semi-minor axis) of 6, and 13 for an aspect ratio of 4. These results compare to a factor of 12 to 14 at the forehead reported by Silva et. al., (1985) and a factor of 18 reported by Kaune and Phillips (1980), both for ac fields. However, the calculated field intensification on axis, at a distance of 20 cm above the top surface of an ellipsoid with semi-major axis 2 m, was between 3 and 3.5, and not sensitive to aspect ratio, in agreement with observation.

The field intensity observed over the head was reduced to 9 kV/m when the subject was wearing a plastic hard-hat, and with no other change. This reduction is thought to be a result of charge deposited on the dielectric helmet. It appears likely that the electric field around a human subject can be modified by charge deposited on the hair and clothing by a dc ion current. The presence of charge on the hair was clearly observed on several of the investigators during the course of these measurements.

WITHOUT HARD-HAT

9.2
20.8

WITH HARD-HAT

25.6 →   ← 20.0

21.2 →
19.2 →   ← 14.4

                ← 11.6

16.8 →   ← 8.8

13.6 →
8.0 →   ← 6.0

                ← 4.0

5.2 →

                3.6
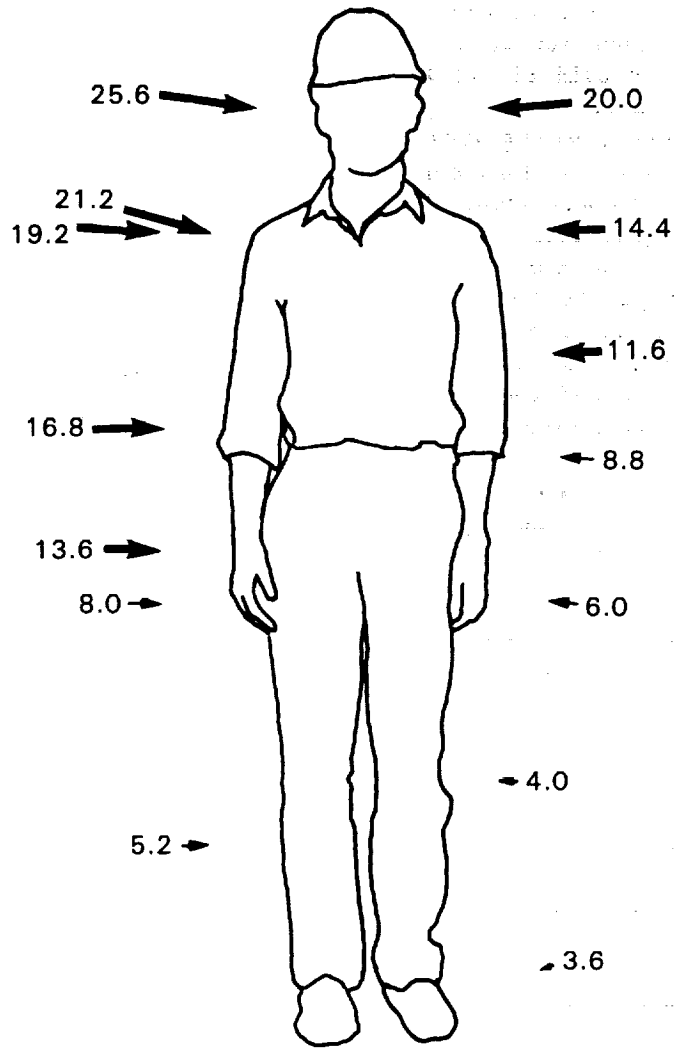
Figure 2-14.   Electric Field Vectors Measured Near a Test Subject
(Measurement Point Is at Head of Arrow)

2-26
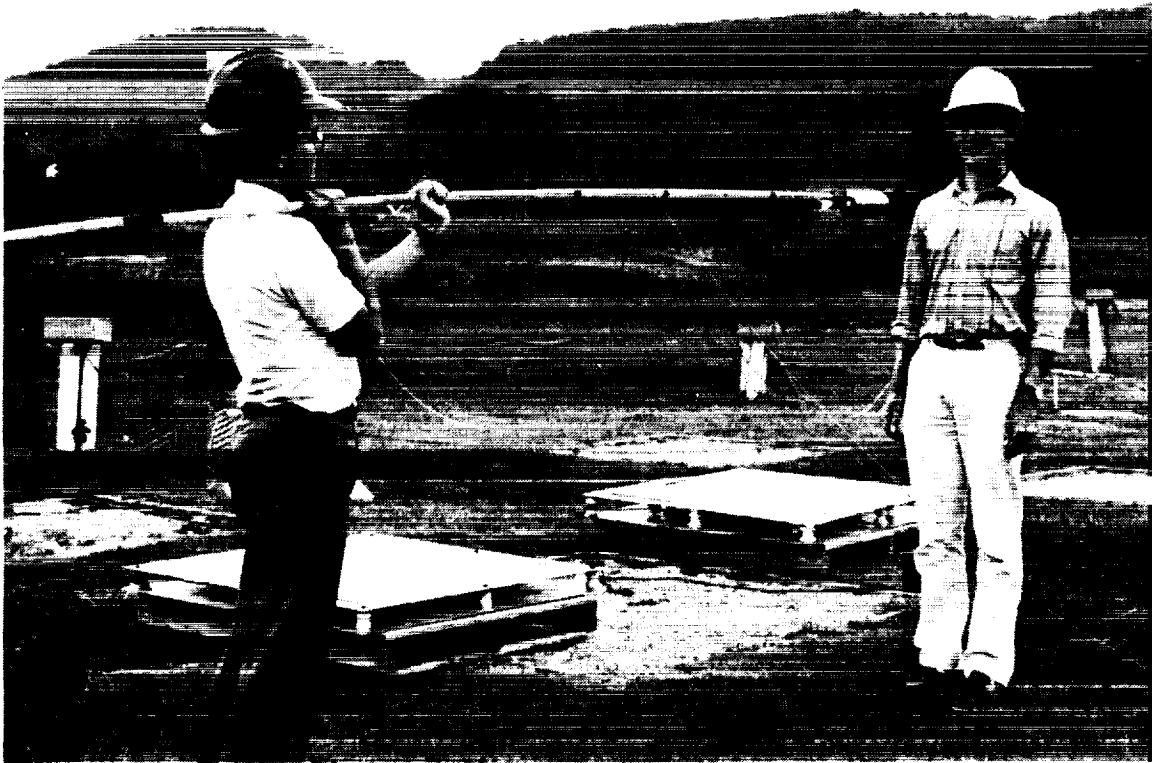
Figure 2-15. Measurement of Electric Field in the
Vicinity of a Person

The third set of data, shown in Figure 2-16, shows the response of the sensor as a function of time, at a fixed location directly under the dc conductor and 0.6 m above the ground surface. The conductor voltage was changed from -200 kV to -500 kV during the interval between the one minute and the two minute marks in the figure, and remained constant after that.

The field at ground level as measured by the HVTRF instrumentation is also shown in the figure for comparison. The ion current, also measured by the HVTRF instruments, varied between roughly 20 and 170 nA/m^2 during the period of measurement, the changes being due to a light and variable wind transverse to the test line. The magnitude of the ion current that would have been collected and measured by the field probe, if it had been grounded, was about three orders of magnitude smaller than the current induced by the electric field. Changes in the field with time, as measured with the two instruments, correlate well. The prototype sensor yielded a lower field value by about 15%, on the average.

Similar observations were made by Maruvada et al.,(1983) using two independently calibrated instruments, one a ground plane field mill, and the other a large split cylinder probe. He also observed a lower field, by approximately the same amount under the same test line at the HVTRF, although another comparison involving several instruments shows no similar systematic difference for all the instruments (Comber et al., 1983).

A number of possible error sources were examined during analysis of the data, but none were found to be large enough to explain the observed difference. These included error due to self-charging of our prototype sensor, either in the calibration cage or under the test line, charge accumulation or leakage along the fiberglass supporting pole, and instrumentation errors.

To calibrate the HVTRF fixed-location field meters, a vibrating plate electrometer, mounted in a 1 m^2 plate, was first calibrated in the test cage and then placed on the ground adjacent to the fixed instrumentation, where it was used as a transfer standard. It is felt that the 15% difference between the prototype sensor and the HVTRF instruments may represent a nonuniformity of the field near the ground surface in the measurement area, including the temporary location of the transfer standard. To illustrate this explanation, Figure 2-17 shows the field intensity as measured 0.6 m above the ground surface along a line parallel to the HVDC conductor and crossing the line of instrumentation.

The horizontal scale in the figure is approximate, but the relative location of the elements of the HVTRF instrumentation is correctly noted. Variations in the electric field of the required magnitude are seen, especially over the slightly raised ion current sensing plates, as expected. These variations cannot be due to self-charging or calibration errors in the isolated-probe sensor. However, if the effective ground plane surrounding the transfer standard were depressed below the 1 m^2 aluminum plate in which it was mounted, or if a local depression of the effective ground existed under our prototype sensor, distortion could occur that would explain the discrepancy.
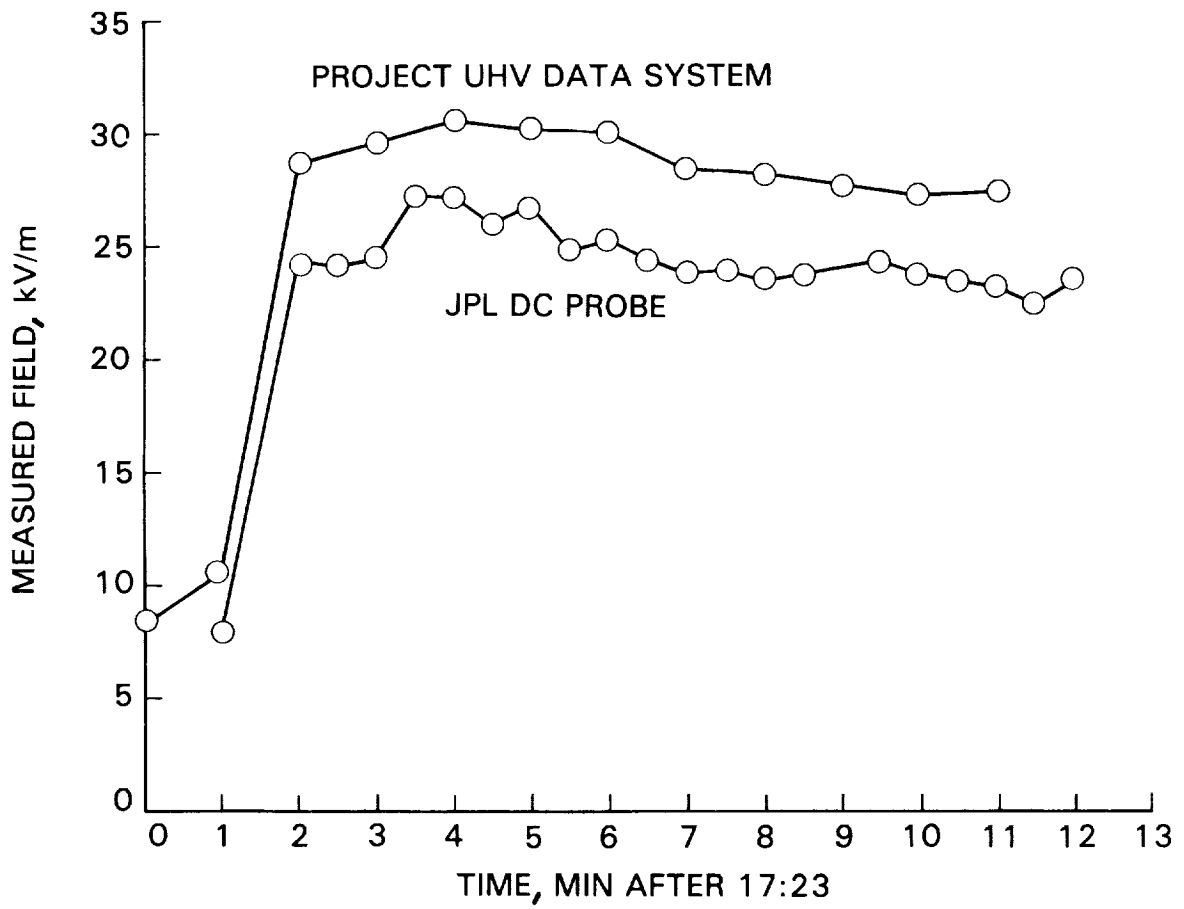
Figure 2-16.   Electric Field Versus Time Measured Under DC Conductor,
Compared to HVTRF Data
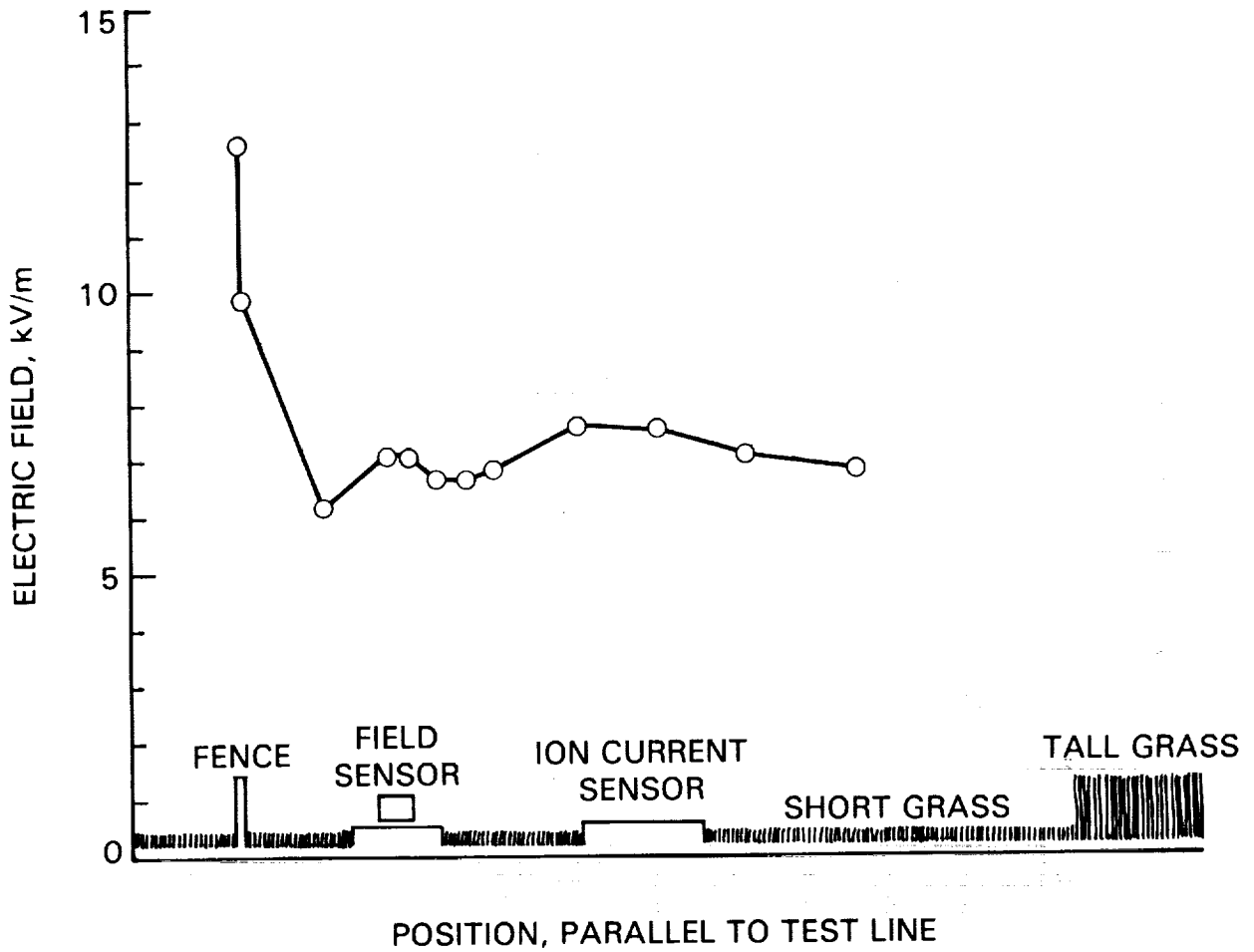
Figure 2-17. Measured Field Values Along a Line Crossing Permanent
Instrumentation, 0.6 m Above Ground

2.3.7   SELF-CHARGING EXPERIMENTS

A detailed investigation, both analytical and experimental, of the effects of self-charging of the sensor is underway, with the goal of understanding quantitatively the errors induced by charge accumulation in a space-charge environment.

The space around high-voltage conductors where field measurement is likely to be of interest normally conducts a significant ion current. The sensor is electrically isolated in order to allow field measurements far from the ground plane. This combination of an isolated sensor subjected to space charge current has not been previously analyzed.

The parameters of interest are, first, the influence of a conducting surface near the sensor, and second, the potential of the sensor itself, or more precisely, the potential difference between the sensor and the free space potential at its location. This voltage difference will be referred to as the excess voltage of the sensor. The dc sensor described above was placed in a specially configured test cage for experimental measurements, and theoretical calculations to confirm the results are still in progress.

2.3.7.1   Experimental Test Arrangement

Before the dc sensor could be evaluated for the effects of self-charging, a means of producing a uniform dc electric field with negligible space charge was needed. A test cage arrangement similar to those used elsewhere to calibrate ac field strength meters was designed and constructed. This arrangement consists of two parallel electrodes of equal size separated and supported by dielectric rods.

The dimensions of the test cage and clearance distance between the cage and surrounding conductors was determined after taking into account published material by Takuma, Kawamoto and Sunga (1985) which analyzed field variations within a test cage. The dimensions selected for our test cage are expected to keep distortion to within 2% at the sensor location.

The field cage was made from two 6 ft by 6 ft aluminum screens, separated by one meter. This assembly was supported one meter off the ground, and at least one meter away from any surrounding conductor. Additional dielectric supports outside the cage were used to prevent the screens from sagging, since significant deviations from a uniform field would otherwise occur. Sharp edges and corners of the screens were coated with silicone rubber to eliminate corona.

The upper screen was connected to a variable negative 50 kV dc supply via a feed line parallel to and in the same plane as the screen. The lower screen was similarly connected to a variable reversible polarity 30 kV dc supply. Screen potentials were carefully monitored using separate high voltage probes. With both supplies adjusted to their maximum output, corresponding to a 70 kV/m field, no noticeable corona was observed. The test cage and the sensor mounted in it are shown in a photograph, Figure 2-18.
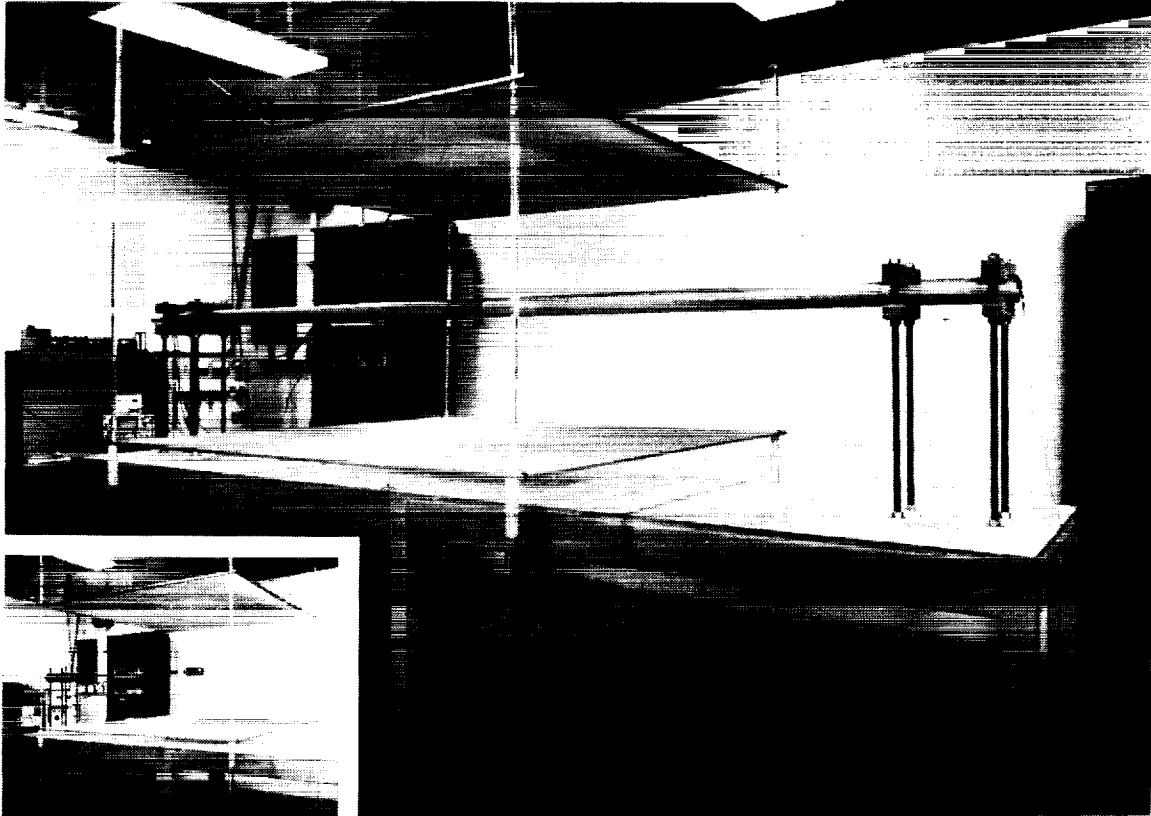
Figure 2-18. Field Cage and Test Bench Arrangement
(Inset Shows Sensor Without Tubes)

A special test bench, seen in Figure 2-18, was constructed to support and manipulate not only the sensor by itself, using its fiberglass support pole, but also to hold two stationary 6 ft aluminum tubes extending from each end of the sensor. These tubes, which have the same diameter as the sensor, were adjusted to be coaxial and within 3 mm of each end of the sensor to approximate the infinite cylinder geometry treated in the analysis.

2.3.7.2   Parameter Measurements

Prior to the self-charging experiments, a linearity test of the sensor output versus electric field was made. The sensor was positioned in the center of the cage (without the tubes) while its output was measured for fields ranging from 1 to 60 kV/m. Within the above range the sensor was linear to within 1%, as shown in Figure 2-19.

With the cylindrical tubes added to the arrangement, measurements were taken with the axis of the sensor at different distances above the bottom screen, ranging from a minimum of 1.2 sensor radii to a maximum of 13.1 radii at the center of the cage. During these measurements, the extension tubes and the sensor were both grounded to ensure that its potential was known. The connection to the circuit ground on the rotating electronics package was made by means of a brush and slip-ring assembly.

While maintaining the field in the cage at 30 kV/m ±1%, the variable supplies were manipulated to create different excess voltages at the sensor. Figure 2-20 shows how one such excess voltage was produced.

Figure 2-21 shows the observed variations in sensor output as a function of excess voltage and distance from the lower plane of the cage. In the case where d/r is 1.2, the gap between sensor and conducting plane is only 0.2r. As can be expected in this case, measurement error due to field distortion between sensor and plate is large. In the case where d/r is 5.25, the surface of the sensor is 16 cm above the conductor (or about 6 inches) and the error has been reduced to less than 10%, even with excess voltages as great as 2kV.

From the data above, graphs were made which plot fractional change in sensor output as a function of d/r, both for an uncharged sensor (excess voltage zero) and for a sensor charged to an excess voltage of -2.64 kV. An excess voltage of -2.64 kV was determined through preliminary finite element calculations to be the equilibrium potential to which the sensor would charge in this field if subjected to a space-charge current. Figure 2-22 and Figure 2-23 show some of our measurements.

The entire experimental procedure described above was repeated with the extension tubes removed. The only observed difference was an increase in scale factor of approximately 25% when the extension tubes were removed. The two factors creating this increase are field fringing in an axial direction at each end of the sensor, and the effect of the curved anti-corona shells on the end of each electrode. Both of these effects increase the effective area of the electrodes. The magnitude of the observed increase in scale factor is in agreement with an analytical estimate.

2-33
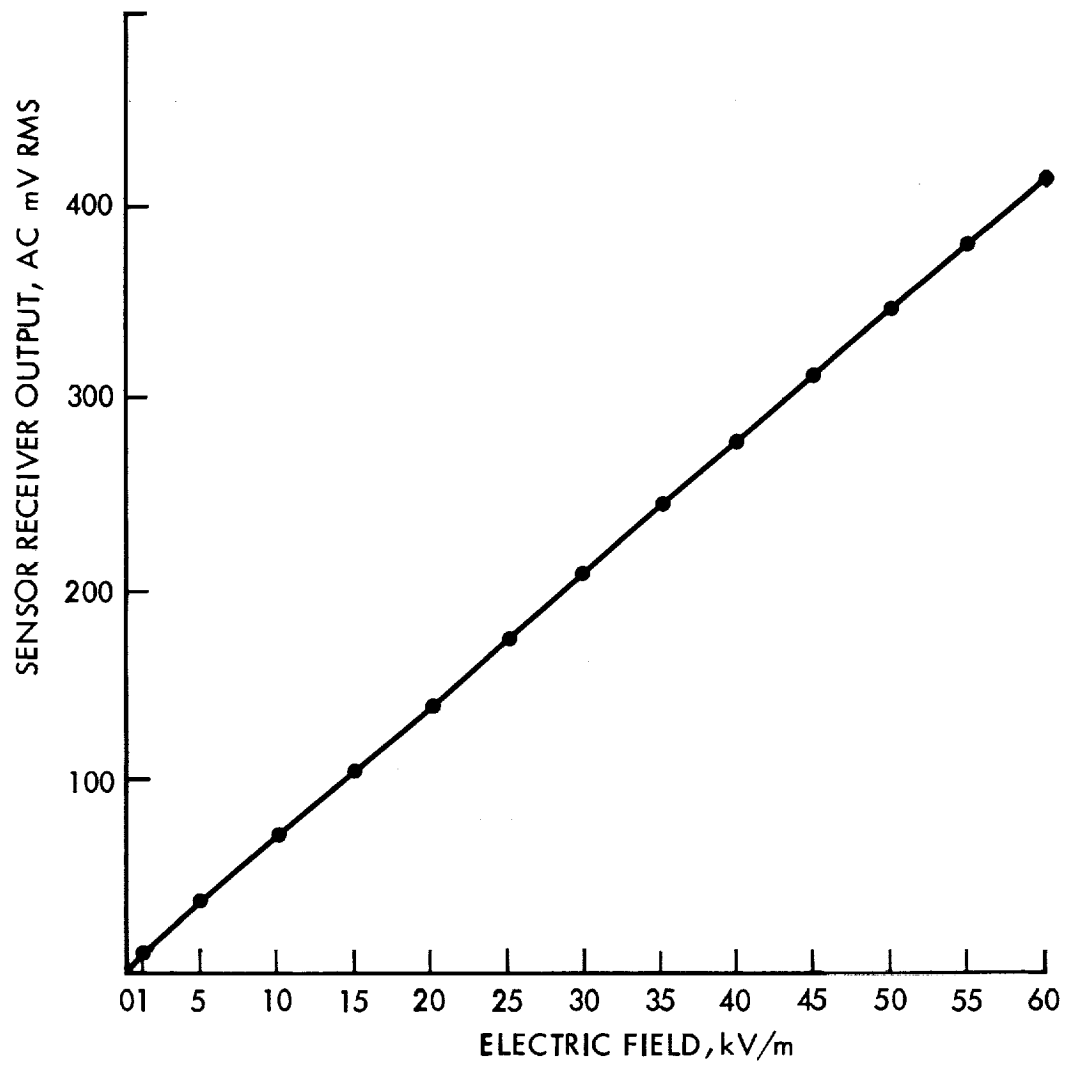
Figure 2-19.   Measured Sensor Output as a Function of Electric Field

UPPER SCREEN $V_1 = -26\,kV$

$\ell = 1\,m$

SENSOR
AXES

FOR $d/r = 2.6$

$r = 3.81\ cm$

$d = 9.91\ cm$

$V_2 = +4\,kV$
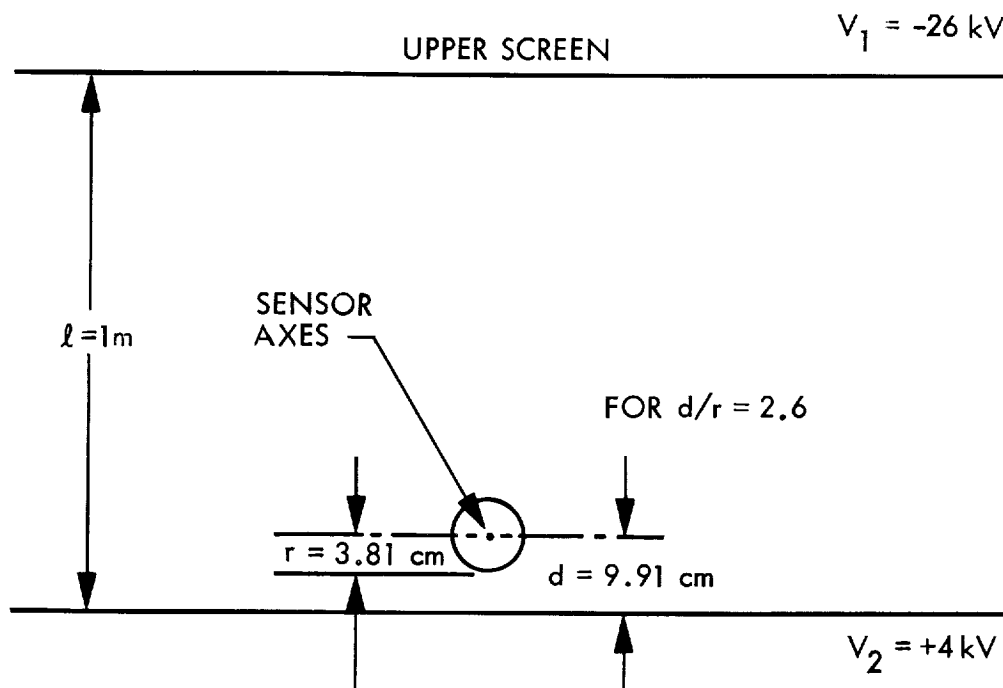
$$\bar{E} = \frac{V_1 - V_2}{\ell} = \frac{-26\,kV - (+4\,kV)}{1m} = 30\,kV/m$$

$$V_{EXCESS} = V_2 - \left[\bar{E}\cdot d\right] = +4\,kV - \left[30\,kV/m \cdot 0.991m\right] = +1027V$$

Figure 2-20. Example Showing Arrangement Used to Produce an Excess Voltage of +1027 V on the Sensor
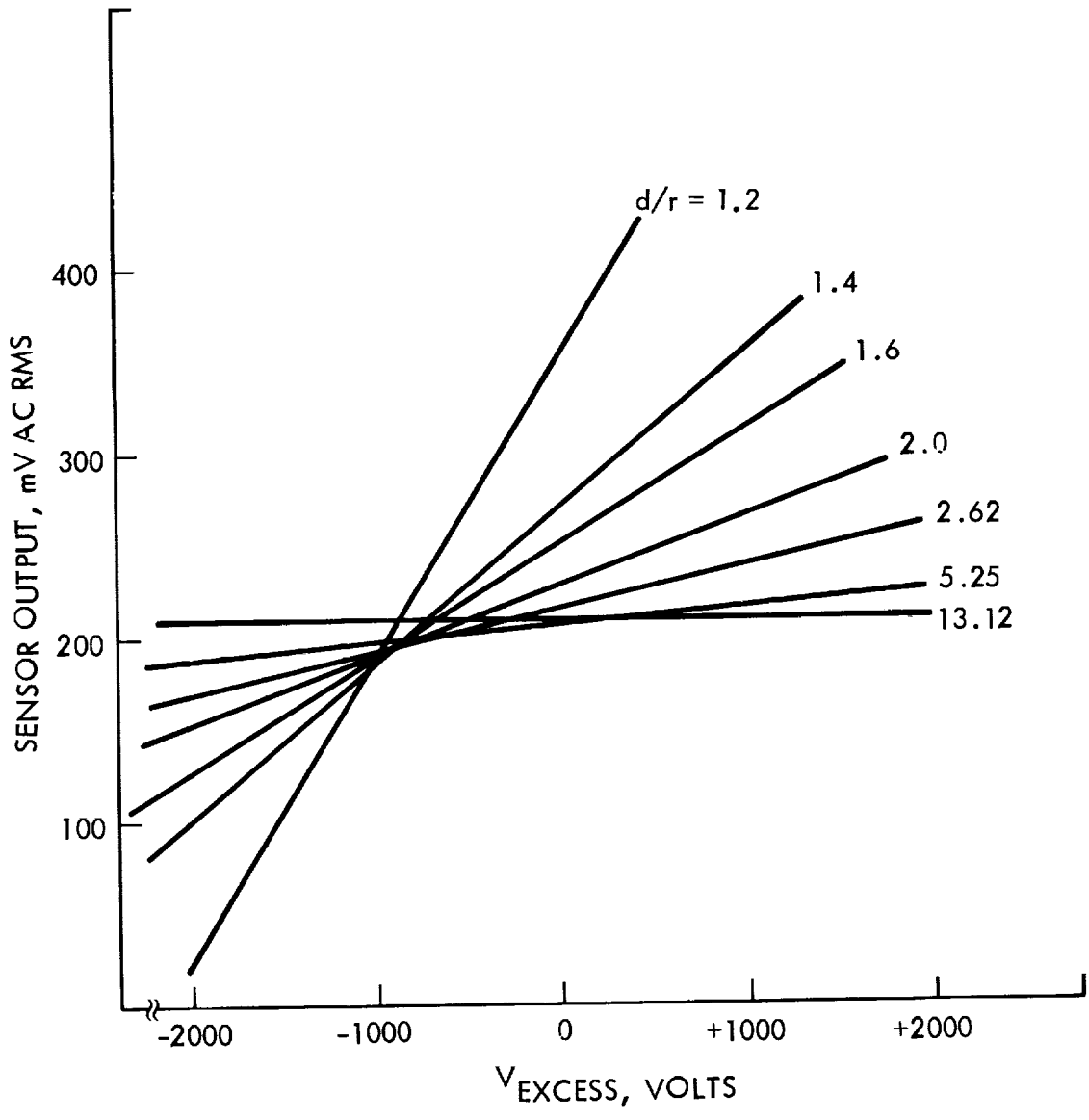
Figure 2-21. Sensor Output vs Sensor Excess Voltage for Various
Ratios of d to r, E Field Constant at 30 kV/m
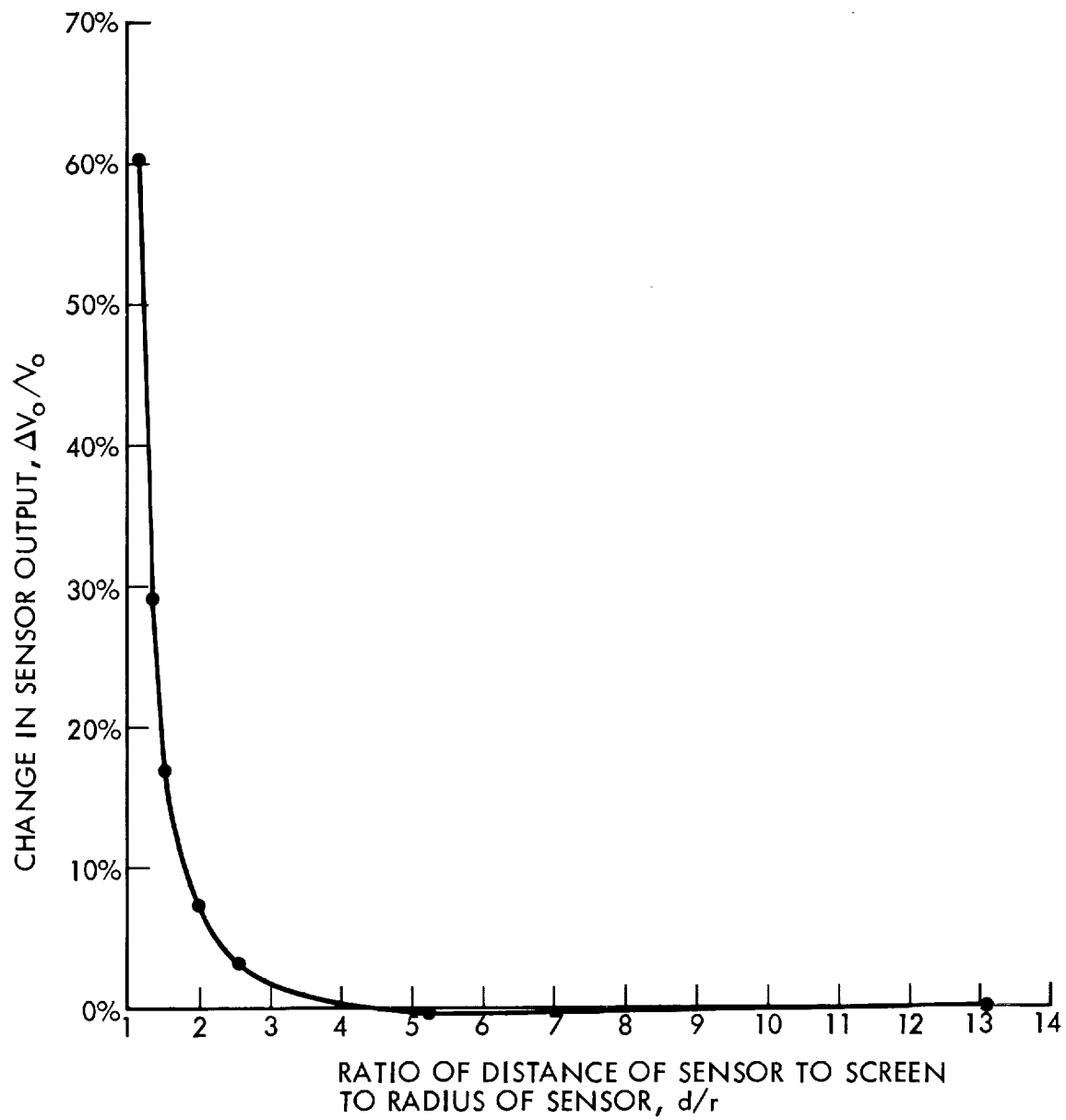
Figure 2-22.   Measured Change in Sensor Output as a Function of
Distance to Screen, Sensor Uncharged
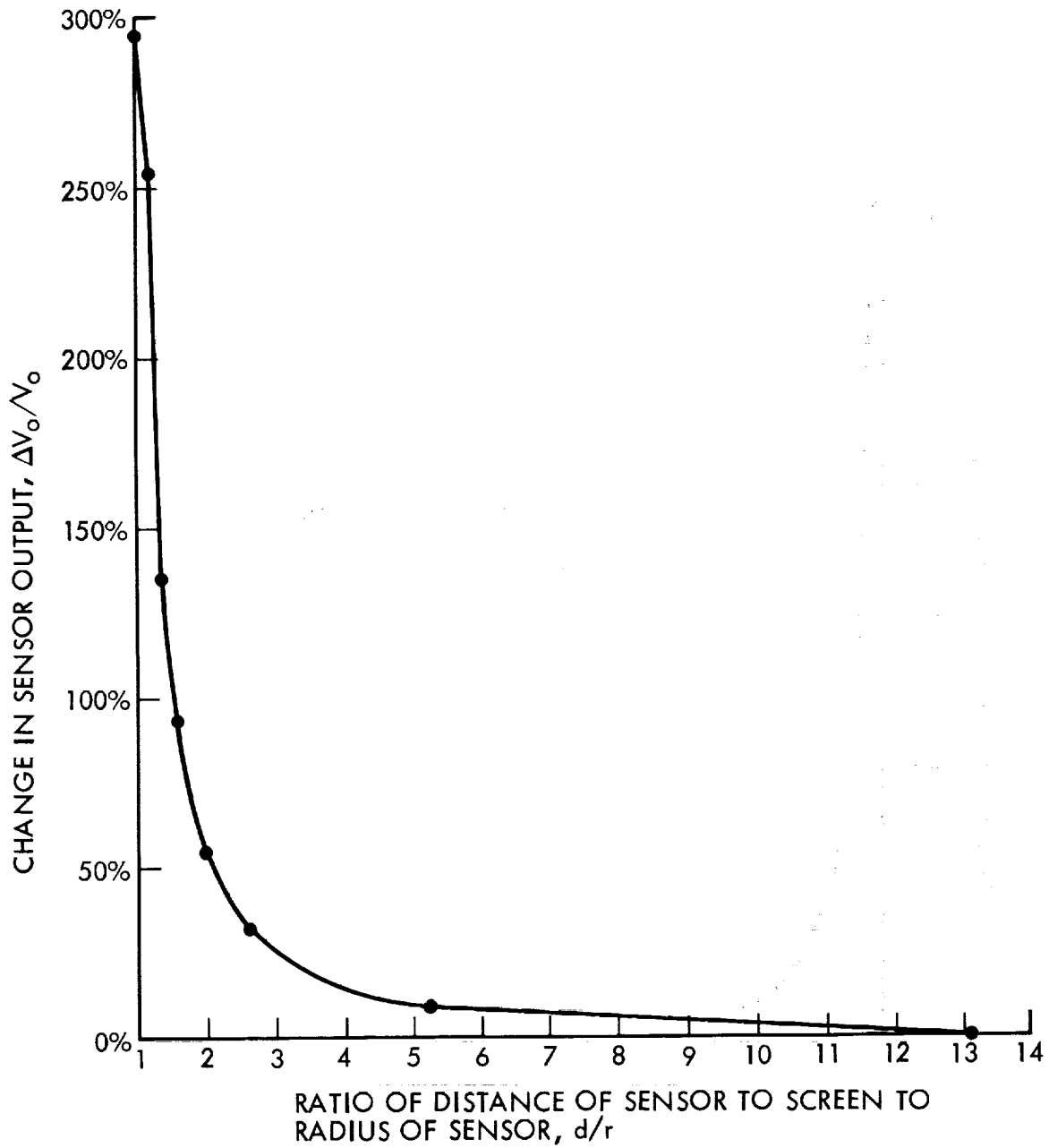
Figure 2-23.   Measured Change in Sensor Output as a Function of
              Distance to Screen, Sensor Fully Charged (-2.64 kV)

2.3.8   CONCLUSIONS

Initial laboratory and field experiments have shown that electric field measurements in free space above the ground plane can be readily made with an electrically isolated probe which is small and portable. Experimental and analytical work to date indicates that readout of induced charge with 2% accuracy will be readily achievable, and that image fields due to self-charging in the presence of nearby conductors will not unduly limit accuracy. In addition, it was possible to measure the electric field vector, that is, both magnitude and direction of an unknown field, at locations above the ground plane with the sensor.

It should be noted that the same sensor has been used to measure ac (60 Hz) fields simply by stopping the spin and reading out the 60 Hz component of the output signal. Field direction for an ac field could be determined from the internal position reference with appropriate instrumentation using, for example, a spin rate small compared to 60 Hz (say, 80 rpm). Experimental results obtained in ac fields will be reported on later.

Further work on this sensor will focus on refinement of the sensor design, with the goal of reducing the size and easing the requirement for frequent battery change. Analysis indicates that the induced charge can be detected with adequate accuracy on an electrode area as small as 1 cm^2 with good electrometer amplifier design. For example, referring to Equation 2, with applied field E_o = 100 V/m, a = 0.5 cm, 1 = 2 cm, and ω corresponding to 20,000 rpm, the field-induced current i_c is 1 nA, well within the reach of good semiconductor electrometer amplifier design.

SECTION 3

FIBER OPTIC TEMPERATURE SENSING

One area where fiber optics can make possible a power system measurement that has not previously been made is the distributed sensing of temperature in electrical apparatus. There are three areas within power systems where such a measurement would be of considerable value: overhead phase conductors, underground cables, and station equipment. Each of these areas will be discussed in turn.

3.1   APPLICATIONS

3.1.1   Overhead Phase Conductor Temperature Measurement

Since any electrical conductor at normal temperatures has a finite resistance, the current that it transmits causes it to dissipate heat. The temperature of a heavily loaded phase conductor varies according to the wind speed and direction, and according to the current that it is carrying. Because of this, it probably varies from span to span. The hottest span in the line (wherever that may be) determines the thermal rating for the line. Since the hottest span is not, in general, known during operation of the line, the thermal rating is based on a statistically developed table of line capacity against ambient temperature. This is, of necessity, somewhat conservative.

If a fiber optic cable could be installed so as to measure the temperature along the phase conductor, it would be possible to develop a dynamic thermal rating system. A system of this sort would allow the line ampacity to be determined accurately based on measurement. This would result in improved utilization of equipment, and, therefore, of the capital investment associated with the equipment.

To be of maximum use, the fiber optic cable has to be installed on existing conductors. This can be accomplished by placing the fiber optic cable around the existing conductor, probably within a tube of plastic. The relation between the temperature seen by the fiber and the temperature inside the phase conductor would have to be determined carefully.

The use of small objects wrapped around the larger phase conductor in this way has been likened to the action of a aerodynamic spoiler, and is said to have advantages in terms of controlling aeolian line vibration and ice galloping.

Overhead lines frequently go for distances in the order of 50 kilometers without being tapped, and, consequently, a temperature measurement system must be able to reach distances in this order of magnitude. It will be seen later that this tends to limit the number of ways in which temperature can be measured.

3.1.2 Underground Cable Temperature Measurement

Knowledge of the temperature distribution along an underground cable offers potentially the same benefits as it does in the case of an overhead conductor. The circuit can be operated closer to its thermal limit in the steady state, and emergency operation at higher temperatures may be possible, since the ability of an underground cable to carry an overload is strongly dependent on the temperature when the overload begins. Unlike the case of an overhead conductor, however, which will sag as it gets hot, the underground cable is supported along its length, and cannot move at all. However, operation at high temperatures is known to degrade the insulation and shorten its life. Under present circumstances, operation of cables is perhaps even more conservative than overhead lines.

There is considerable interest in knowing the temperature profile of pipe-type cables, in which the three phase conductors separately are inserted into a pipe filled with dielectric fluid (oil). A knowledge of the temperature profile along the line will permit the evaluation of the effectiveness of attempts to improve the cooling by circulating the oil, or other measures.

Normally pipe-type cables are spliced at distances not in excess of two kilometers. Consequently, a system of temperature measurement might only have to reach that distance.

3.1.3 Power System Equipment Temperature Monitoring

There are a number of potential applications for fiber optic temperature monitoring inside power system equipment. Of particular interest are measurements which will enable the determination of winding hot spots in transformers and reactors, and the temperature distribution of surge arrestors.

In new transformers, the fiber could be integrated with the winding or incorporated in the winding duct spacer. In existing units, the fiber could be threaded through the cooling ducts or placed on the outside of the winding.

The exact location of the fiber would also influence whether the fiber was exposed to an electrical stress as well as temperature effects. This in turn might affect the method chosen for the measurement.

The distance that would need to be monitored for an understanding of the temperature distribution inside a piece of power system equipment is the shortest of the three applications considered here. It would probably not exceed a few tens of meters even if the fiber were wrapped around the transformer winding a few times.

## 3.2 METHODS OF MEASURING TEMPERATURE DISTRIBUTION

In order to measure any parameter (including temperature) as a function of distance, some form of reflectometer is needed. A reflectometer can be thought of as a kind of radar operating down the optical fiber. Radar of the kind used at airports operates in free space. The velocity of radio waves in free space is a constant. It is therefore possible to calibrate the radar reflections in terms of their distance from the transmitter. The reflection of a pulse a certain time after it was transmitted yields directly the distance to the object which caused the reflection.

In cables, whether optical or radio type cables, the velocity of transmission is lower than the velocity of light in free space, and the calibration in terms of distance is more difficult, although, in principle, if all the parameters of the cable are known, it can be done. For this reason, reflectometers operating in cables are conventionally referred to as time-domain reflectometers. In fiber optics, since the pulses are optical rather than of radio wavelengths, the device used is known as an optical time-domain reflectometer.

An optical pulse launched into a fiber will be transmitted through it almost unchanged for the entire length of the fiber. It will be slightly changed, however. At any particular position there will be some reflection of the energy in the pulse. Some of the energy is scattered by the molecules of the glass, a phenomenon known as Rayleigh scattering. (The energy returning to the sending end in this manner is said to be backscattered.) This effect, while small, does mean that the pulse is slightly attenuated as it proceeds down the fiber. The curve of reflected power (measured by the OTDR from the backscattered energy) as a function of time (or distance) as seen on the display of the OTDR will, therefore, inevitably show some droop. Any discontinuity in the fiber will show up as an excess loss over and above this normal droop. In this way, it is possible to test the quality of splices and connectors in fiber optic systems, an application in which the OTDR is invaluable. Figure 3-1 shows an OTDR system and its output from a sample cable.

Another way in which the pulse launched into the fiber is changed during its transmission is its tendency to spread out due to the various kinds of dispersion occurring in the fiber. (See Kirkham et al. (1984) for a detailed explanation of dispersion.) In an ordinary telecommunications application, dispersion limits the bandwidth-distance product of the fiber, that is to say, it provides an upper limit on either the distance or the bandwidth for which the fiber can be used.

For our application in measuring the position of a hot spot, dispersion will limit the accuracy with which the position of any discontinuity in the fiber can be determined. Based on the approximation that in free space light travels about one foot in one nanosecond, one can develop the rule of thumb that a pulse which is spread to a microsecond in width in an optical fiber cannot give the location of any discontinuity to an accuracy better than a few hundred feet.
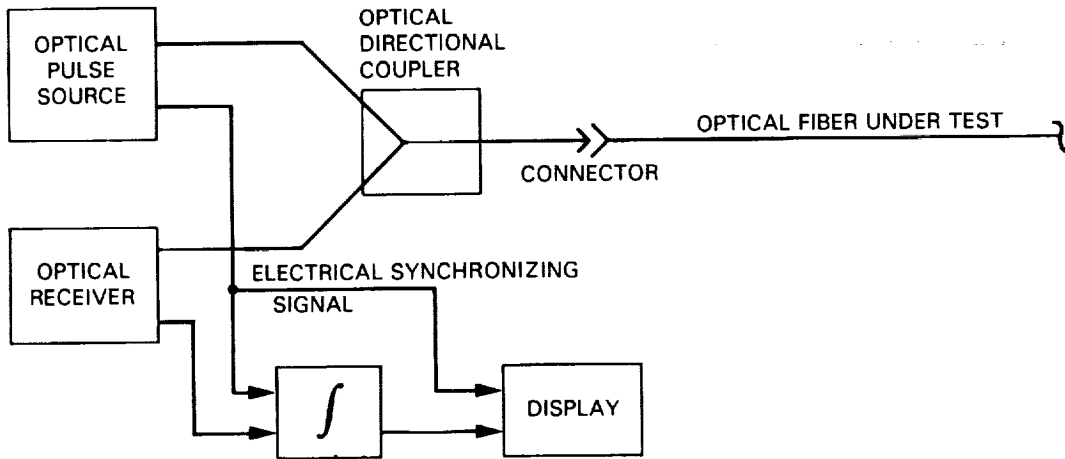
a) Optical Time-domain Reflectometer
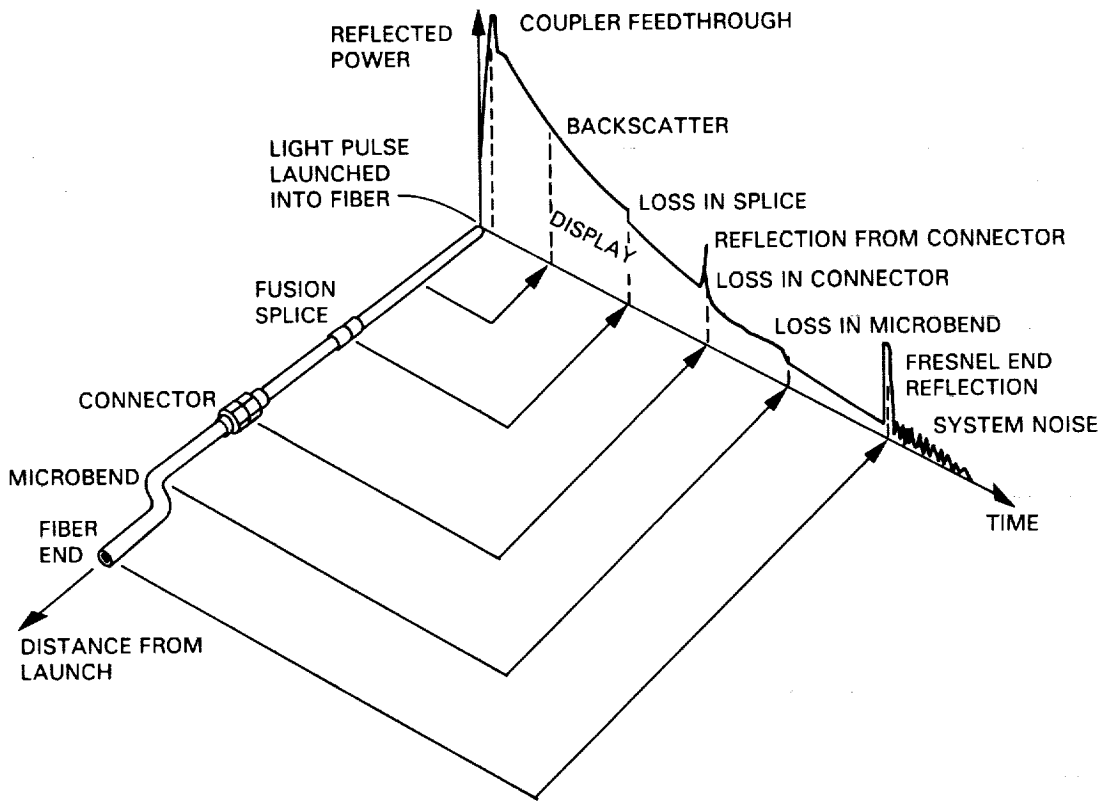
b) OTDR display

Figure 3-1. Optical Time Domain Reflectometry

To obtain the temperature profile of a fiber, the OTDR display can be used to show temperature as a function of distance, rather than loss as a function of distance. To do this, the temperature must be related to the loss, or to some form of reflectivity, in some known way. The OTDR display could then be calibrated directly in terms of temperature. Temperature resolution is set by the ability of the OTDR to distinguish between two values of loss. A reasonable value here is 0.1 dB.

Distance resolution is a function of the width of the pulse launched into the fiber, and the dispersion. Since the effects of dispersion increase with distance, the resolution will deteriorate with 'reach' for a given OTDR. For a 2 km reach, a resolution of 10 nsec (about 3 m) should be possible, depending on the fiber.

Distributed temperature can be sensed through a number of possible mechanisms using an optical time-domain reflectometer. These include temperature dependence of birefringence, temperature dependence of losses, coupling variations with temperature, temperature dependence of core-cladding index ratio (or numerical aperture), optical effects in temperature sensitive compounds (particularly organic compounds), and simple temperature dependence of optical index. Each of these approaches will be discussed in turn.

3.2.1   Temperature Dependent Birefringence

Certain materials exhibit a different refractive index for two orthogonal polarizations of light. Materials exhibiting this property are said to be birefringent. Normally, one considers two orthogonal linear polarizations, one exhibiting the fastest propagation velocity in the material and the other (orthogonal to it) exhibiting the slowest propagation velocity. If the birefringence can be made temperature dependent, then, in principle, the temperature can be sensed along the fiber. The different transmission velocities of the two orthogonal components will result in their having a phase relation which varies as a function of temperature. Analysis of the reflected information for a sensor of this type will be a little more complicated than for a straightforward optical time-domain reflectometer. However, the equipment shown in Figure 3-2 can probably be arranged to provide a readout of temperature as a function of distance.

Until recently, fibers which preserved the state of polarization were not available. While they are currently being manufactured, the temperature dependence of the birefringence has not been investigated. Therefore, while this approach, at least in concept, can give a temperature distribution sensor, it must be regarded as somewhat high risk at this point.

3.2.2   Temperature Dependent Loss

Normally, the glass used in making a fiber is extremely pure, because impurities have been found to cause loss of optical power. By deliberately doping the glass with a suitable material, however, it is possible to construct a fiber in which the loss varies as a function of temperature. This may be the simplest method of measuring temperature, and may require the least

BEAMSPLITTER

POLARIZED
SOURCE

POLARIZATION
ANALYZING
DETECTOR

PROCESSOR

PHASE RELATION OF ORTHOGONAL
POLARIZATIONS DEPENDS ON
BIREFRINGENCE
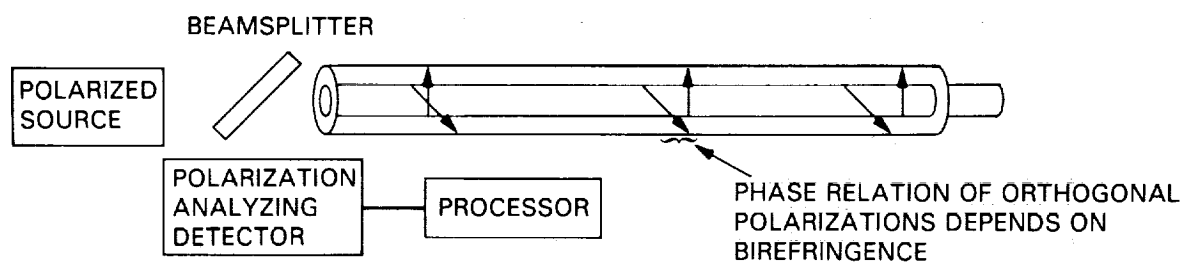
Figure 3-2.   Birefringence Sensing

development. The transition metals, such as Cu, Fe, Ni, Co, and Cr have ions
that will absorb photons at the visible and infra-red wavelengths of interest.
Doping with one of these materials would seem like a reasonable place to
start.

As explained in an earlier JPL report (Kirkham et al., 1984) microbending
represents an excess loss in many fibers. In some implementations of
microbending sensors, the bare fiber stripped of buffer is deliberately
exposed to pressures from a micro-anvil which causes the loss. In the
anticipated implementation of a temperature dependent microbending loss
sensor, the buffer remains on the fiber and is deliberately made to have
different physical temperature sensitivities than the fiber itself. As a
result of this, a temperature change in the buffer/fiber system induces a
mechanical force on the fiber which results in the required excess loss. The
arrangement is shown in Figure 3-3.

While excess loss of this type has been observed, for example, in some of the
early communications fibers, its mechanism is not well understood and has not
been investigated thoroughly. It might be fair to say that the effect was
observed as a nuisance in the early days of communications fibers. Subsequent
work done on it was aimed at reducing or eliminating its effects.

3.2.3   Coupling Variations With Temperature

If two fibers are run in close proximity for a considerable length, some of
the energy initially launched into one fiber will be coupled into the other.
By choosing the appropriate physical construction, the degree of coupling can
be made temperature dependent. The implementation then becomes a variation of
the basic optical time-domain reflectometer in that the energy is launched
into one fiber and the reflections are received from another.

It is possible to implement the arrangement in a number of ways, one of which
is shown in Figure 3-4. For example, a multicore fiber can be constructed, or
two separate fibers can be encased in the appropriate polymer buffer, or other
combinations of materials can be used.

3.2.4   Temperature Dependent Optical Index Ratio

The efficiency of an optical fiber depends on the ratio of the refractive
indices of the core and the cladding material. Normally, these two parameters
differ only by a few percent. If the refractive index of either the core or
the cladding is made temperature dependent, as in Figure 3-5, then the ratio
between the two, and hence the numerical aperture of the fiber, or efficiency
of transmission, will be made strongly sensitive to temperature. This
variation can be picked up by an optical time-domain reflectometer at the
sending end. Variations in the received power may also be useful in
indicating peak temperatures.

Some earlier work on this approach has been done by Fox (1983) at Oak Ridge
National Laboratory, using an organic liquid core.

POLYMER BUFFER

FIBER

TEMPERATURE
DEPENDENT
FORCE
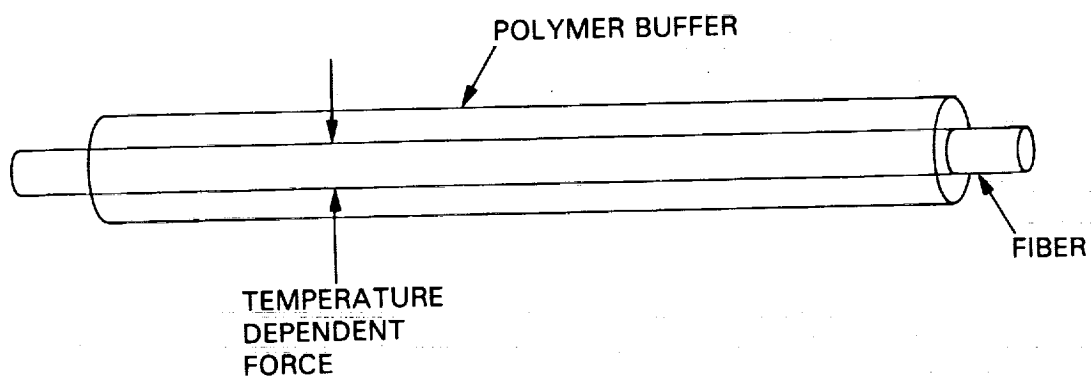
Figure 3-3. Temperature-Dependent Microbending Loss
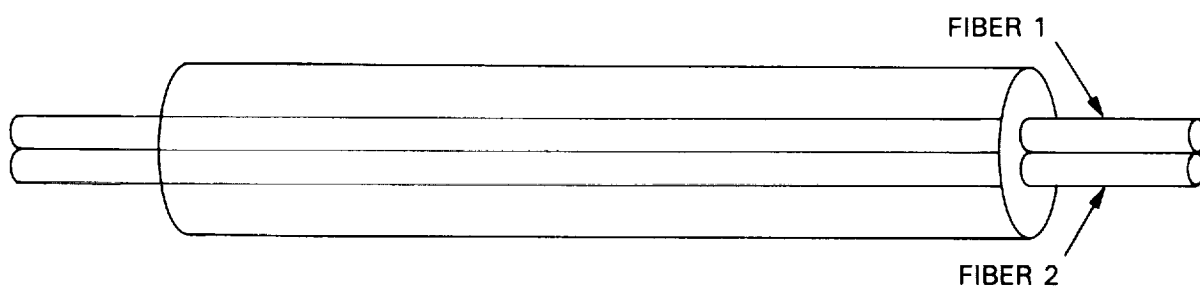
FIBER 1

FIBER 2

Figure 3-4. Temperature-Dependent Coupling

SILICA
FIBER CORE

POLYMER
CLADDING

SILICA CLAD

LIQUID
CORE
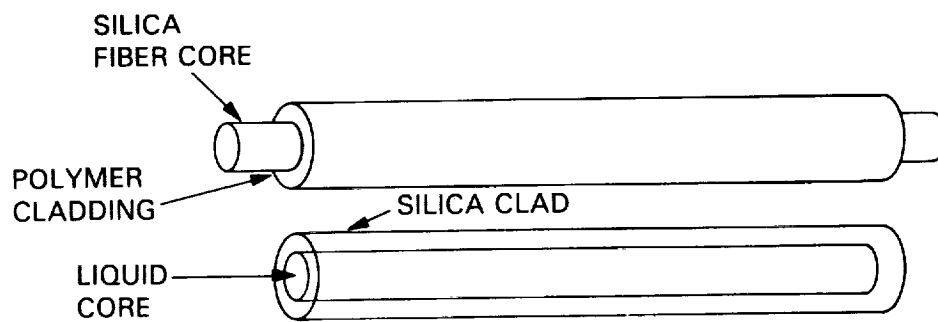
Figure 3-5. Temperature-Dependent Optical Index Ratio

3.2.5   Temperature Dependence of Refractive Index

In all the previous applications of fiber-based temperature sensing, the
distance was estimated on the basis of time.   It is assumed in these
measurements that the propagation velocity through the fiber is known, or can
be estimated, from the refractive index.   An alternative implementation is
possible if the distance is calibrated, for example, by putting a small notch
or other discontinuity in the fiber, say every hundred meters.   Then the
discontinuities can be used to calibrate the propagation velocity or the
change in refractive index.   In an implementation based on this approach, the
transit time between marks which were known to be equidistant would be used to
give an indication of temperature.   Figure 3-6 shows the arrangement.

3.2.6   Point Sensing for Distributed Measurement

There are two other ways in which an optical fiber can be used to give an
indication of temperature distribution.   First, a number of discrete sensors
can be separately interrogated by means of an optical fiber (without using an
optical time-domain reflectometer).   This is shown in Figure 3-7a.
Alternatively, sensors can be distributed down an optical fiber as in
Figure 3-7b, giving the same effect as the previously described distributed
methods.

Implementation of the first approach amounts to using the optical fiber only
as a communications channel.   Each sensor along the fiber can be addressed
separately and the resolution obtained can be arbitrarily defined.   Using this
approach, sensors could be located close together where it was thought that a
hot spot may occur, and far apart elsewhere.

Using the second approach, if the sensors are located close together, they
cannot be individually resolved with a normal OTDR.   The fiber optic then
appears to the OTDR exactly the same as a temperature sensitive fiber.   This
approach has the advantage that a large number of physical effects can be used
to detect the temperature change.

OTDR

FIBER, WITH EVENLY SPACED NOTCHES
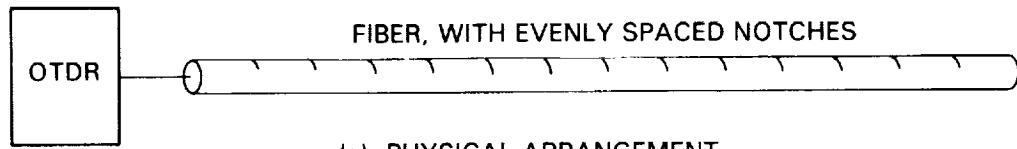
(a) PHYSICAL ARRANGEMENT

REFLECTED
POWER

TIME
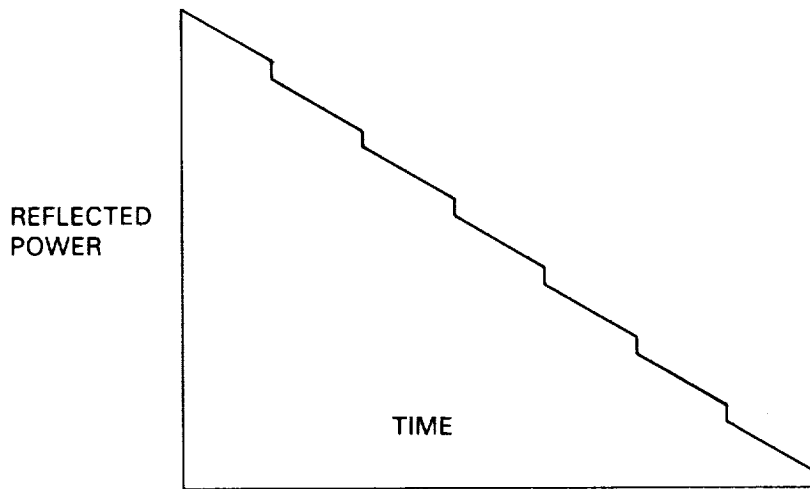
(b) OTDR DISPLAY WITH FIBER AT
UNIFORM TEMPERATURE

REFLECTED
POWER
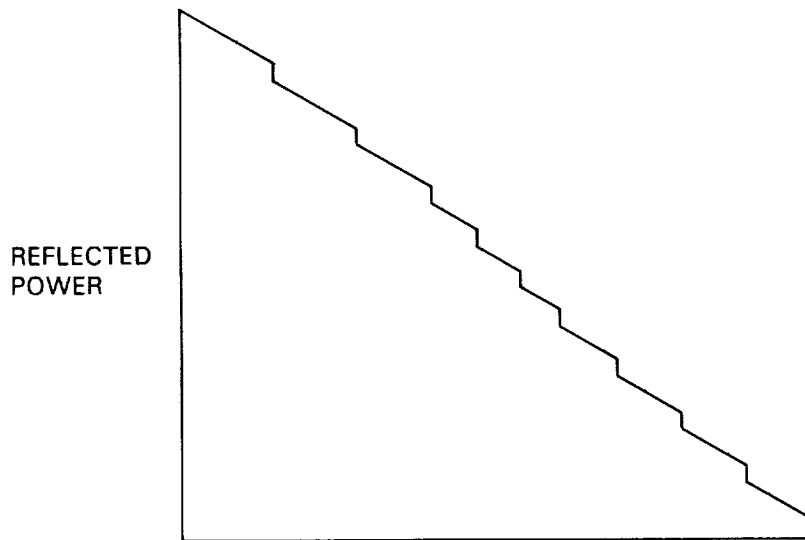
(c)OTDR DISPLAY WITH CENTER SECTION
AT LOWER REFRACTIVE INDEX

Figure 3-6.   Temperature-Dependent Refractive Index
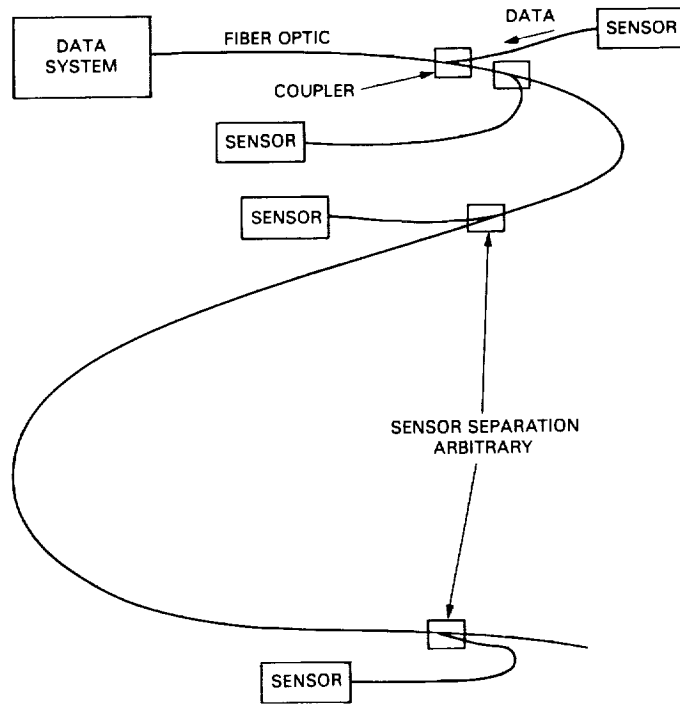
Figure 3-7a.   Separate Sensors Using Optical
Fiber as Communication Channel
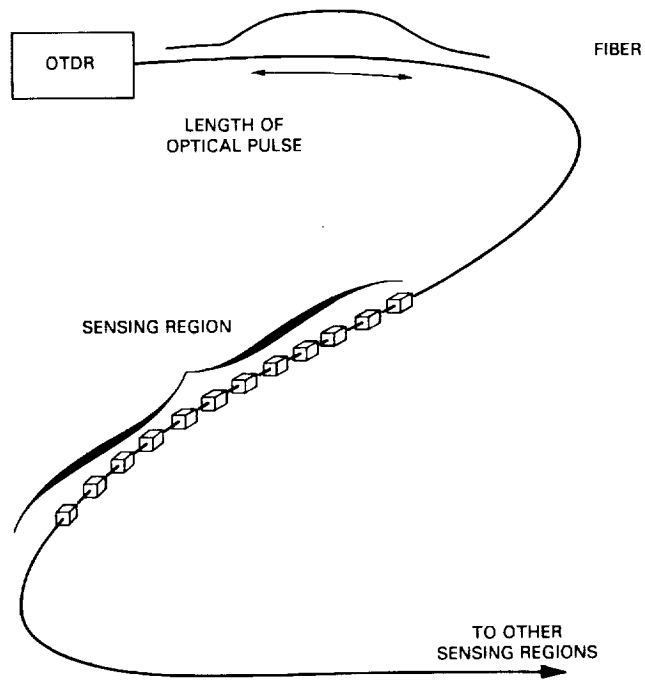
Figure 3-7b.   Separate Sensors Spaced Within the
Resolution of the OTDR

3-13

3.2.7 Distance Reached by a Lossy Distributed Sensor

In this section the capability of a fiber with temperature-dependent loss to measure a temperature change and its location is estimated from first principles. Signal attenuation along a fiber is usually expressed in decibels per unit length, so that the actual input and output power do not have to be specified. Thus, if α is the attenuation per unit length,

$$\alpha = 10 \log \frac{P_{in}}{P_{out}} \qquad (3\text{-}1)$$

The total loss A over a length X of fiber is

$$A = \int_0^X \alpha \, dx = 10 \int_0^X \log \frac{P_{in}}{P_{out}} \, dx \qquad (3\text{-}2)$$

It can be seen that if the loss is constant along the fiber, a length (of fiber) can be calculated at which the loss equals some particular value. This can be used to calculate usable fiber lengths for a particular system signal/noise ratio. If the loss is not constant, the situation becomes more complicated.

If the incremental loss α is made temperature dependent, i.e., if $\alpha = \alpha(T)$, then the loss down a fiber of arbitrary temperature distribution $T(x)$

$$A = \int_0^X \alpha(x) \, dx \qquad (3\text{-}3)$$

can be found by substituting $\alpha(T)$ into $T(x)$. There is experimental evidence for some rather simple functions $\alpha(T)$, such as $\alpha = kT$ or $\alpha = kT^{1/2}$ (depending on the material). To see the effect on maximum length, let us assume that the loss is of the form $\alpha = kT$ so that $\alpha(x) = kT(x)$. For this case,

$$A = k \int_0^X T(x) \, dx \qquad (3\text{-}4)$$

and the solution requires only a specification of $T(x)$. With constant $T(x)$, we obtain the simple result that

$$A = kXT \qquad (3\text{-}5)$$

In practice, OTDR technology is limited in the total loss which can be covered to a value which we will assume to be 30 dB. This means that, for a fiber with positive temperature coefficient of loss, the distance (X), the

temperature (T), and the sensitivity (k) must be chosen together. Some compromise will be inevitable in most applications.

If the required distance is 2 km, and the temperature range of interest is above 60 °C (333K), the sensitivity is limited to

$$k = \frac{30 \text{ dB}}{2 \text{ km x } 333} \qquad (3\text{-}6)$$

$$= 0.045 \text{ dB/km } °C$$

Such a low temperature coefficient of loss would result in a system of low resolution. A 10°C change in temperature for 100 m would produce less than 0.05 dB change in loss. This would be just discernible with 'ordinary' equipment.

One solution is to produce a fiber with a low loss at the lowest temperature of interest, and a greater sensitivity. (This approach might require some exotic material used in the point-sensing approach described above. Nevertheless, it should be workable.)

Suppose, for example, that a fiber is produced that has low loss (say 2 dB/km) at the low end of the temperature range of interest (below 60°C), and a sensitivity of 2 dB/km °C above that temperature.

Suppose that most of a 2-km cable is at 64°C, but a 100 m section near the middle is at 80°C. The total loss can be calculated by modifying Equation 3-5. The two temperature regimes can be considered separately, and their losses added. For each section, a loss rate can be calculated from the basic loss (2 dB/km), the sensitivity and the temperature. Thus

$$A = 1.9 \text{ km x } 10 \text{ dB/km} + 0.1 \text{ km x } 42 \text{ dB/km} \qquad (3\text{-}7)$$

$$= 23.2 \text{ dB}$$

Since the total loss is comfortably below the value set by the OTDR limit of sensitivity, a temperature profile could be obtained.

Suppose, now, that the hot-spot were doubled in length. The total loss is then

$$A = 1.8 \text{ km x } 10 \text{ dB/km} + 0.2 \text{ km x } 42 \text{ dB/km} \qquad (3\text{-}8)$$

$$= 26.4 \text{ dB}$$

which is still a usable value, although it is getting close to the limit.

If the fiber temperature increased by 1°C over its entire length, the loss is given by

$$A = 1.8 \text{ km} \times 12 \text{ dB/km} + 0.2 \text{ km} \times 44 \text{ dB/km} \qquad (3-9)$$

$$= 30.4 \text{ dB}$$

This value exceeds the capability of the OTDR, which therefore would not be able to provide information about the last 200 m (0.4 dB) of the cable.

If the basic temperature and the hot-spot range were known in advance with sufficient precision, a system like this could be made. To achieve the desired resolution, computerized data-taking would be necessary, and the OTDR could be operated many thousands of times to obtain averaged results.

One way in which the system could function would be for the computer to present the results as temperature (computed from loss data) as a function of distance at increments set by the system resolution. If a horizontal resolution of 10 m was achieved, and a loss resolution of 0.1 dB, the temperature resolution would seem to be no better than 5°C. (This result is based on a sensitivity of 2 dB/km/°C.) Temperature and distance resolution can be traded off: either can be improved at the expense of the other. It seems likely that a system of this kind could be arranged to have a loss resolution of 0.01 dB, by means of suitable data processing. The overall temperature profile could then be obtained with a resolution of 10 m and 0.5°C, or 5 m and 1°C. This should satisfy all reasonable requirements.

SECTION 4

OPTICAL POWER TRANSFER

4.1 BACKGROUND

With the development of efficient optical to electrical converters, optically transmitted power could be used to energize electronics for power system measurements. A system powered by optical energy would avoid the need to replenish batteries, or to extract power from power lines. Some work was done on component development at JPL during 1983 and 1984, and is reported elsewhere (Kirkham et al., 1984).

The first experiments performed involved transmitting light over a fiber optic cable, then converting the light into usable electric power using silicon photodiodes. These experiments were performed at JPL using 850 nm wavelength light. The simple diodes used produced only about 0.5 volts (open circuit). This voltage is too low to be useful. Therefore, an array of series connected diodes is needed. Figure 4-1 shows the entire optical power transfer system in block diagram form.

Silicon was chosen in the first experiments because of its availability and easy processing. Unfortunately, unless it is very thick, silicon is not very efficient at converting light at 850 nm to electric energy. If the sample is thick, it would be very difficult to produce a small diode array using integrated circuit techniques. Gallium arsenide (GaAs) is much more efficient at this wavelength, thereby allowing thin layers of material to be used. GaAs was selected for the second set of experiments.

The work done in 1985 was aimed at producing a photodiode array consisting of 32 AlGaAs-GaAs diodes internally connected as four strings of 8 diodes (see Figure 4-2). Although the conversion efficiency for GaAs is much greater than silicon at this wavelength, GaAs has the disadvantage that it is much more difficult to process. GaAs was still considered the better choice because it requires much less material than silicon, making the final array in GaAs smaller.

The diode array was designed using standard integrated circuit design rules. In order to hold the series resistance to a minimum, the diodes were designed as short, wide rectangles. This design resulted in some problems with mask alignment during fabrication. A standard glass photomask set was produced for the photolithographic process.

The diodes were produced using Metal Organic Chemical Vapor Deposition (MOCVD) techniques as follows. A semi-insulating GaAs wafer was used as the substrate that held the individual diodes, and isolated them from each other. A thick layer of n-type GaAs was deposited on this layer, followed by a thinner layer of p-type GaAs. These two layers formed the p-n junction photodiode where the light-to-current conversion takes place. A thin layer of p-type AlGaAs was then deposited as a surface passivation layer. Figure 4-3 shows this sequence of events.

```
LIGHT                                                        OPTICALLY  ──────▶  + V      ⎫
SOURCE ──▶ COUPLER ──//──▶ COUPLER ──▶                       DRIVEN                        ⎪  POWER
(LASER)                                                      POWER      ──────▶  COMMON   ⎬  OUTPUT
                                                             SOURCE     ──────▶  - V      ⎭
   ▲                          FIBER                       ⎣_____⎦
   │                          OPTIC                       LIGHT TO VOLTAGE
 POWER                        CABLE                       CONVERTER
 INPUT
```
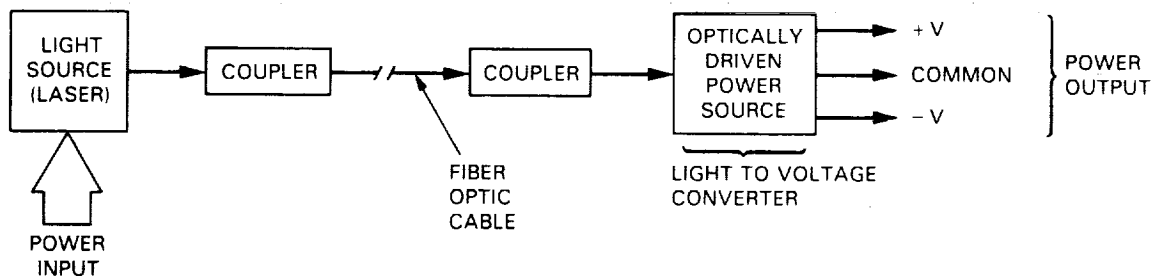
Figure 4-1. Block Diagram of Optical Power Transfer System

4-2
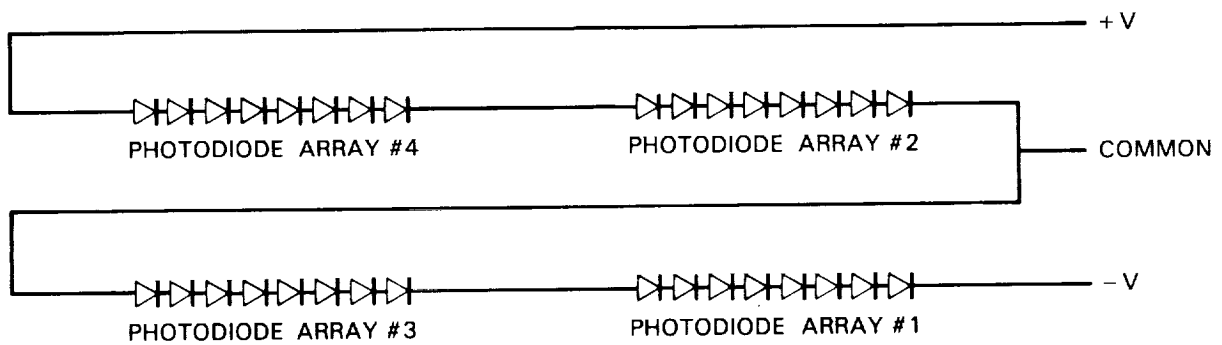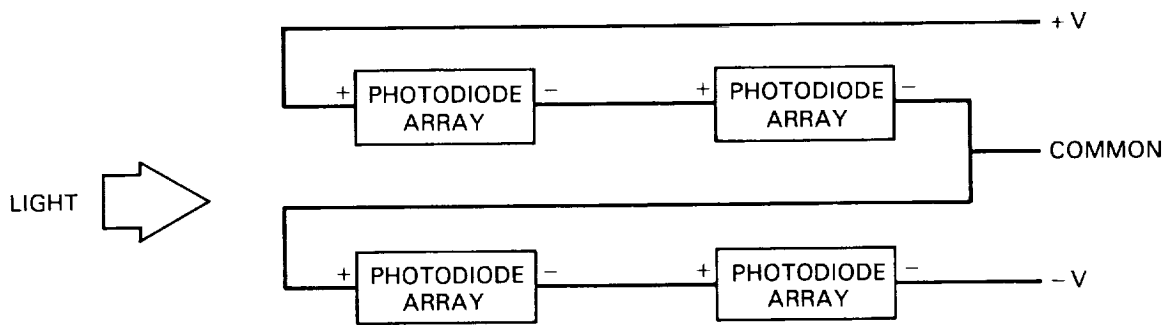
Figure 4-2. Electrical and Physical Arrangement of 32-Diode Array
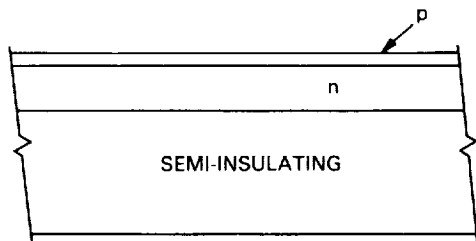
a) SEMI-INSULATING SUBSTRATE WITH
   EPITAXIAL n and p LAYERS
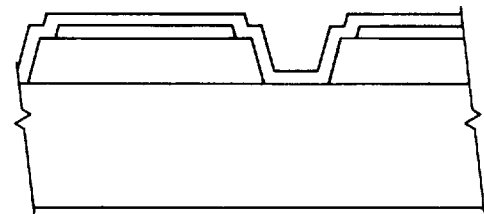
d) OXIDE LAYER SPUTTERED OVER SURFACE
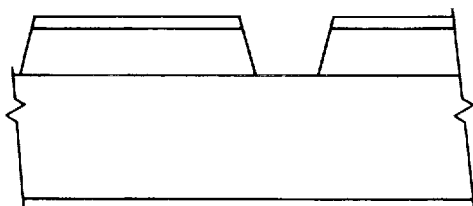
b) ETCHED MESA
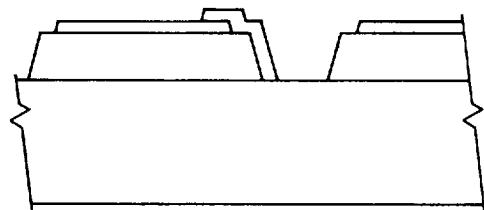
e) MOST OF OXIDE LAYER REMOVED
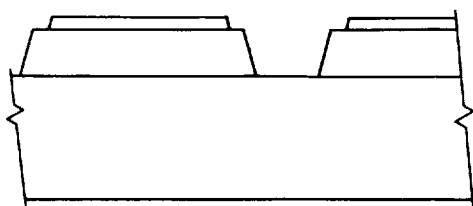
c) SECOND ETCH EXPOSES n LAYER
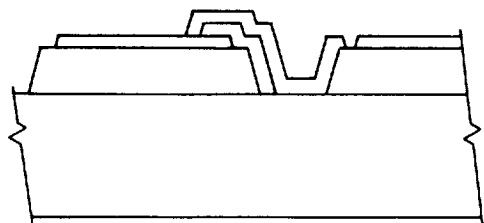
f) SILVER DEPOSITED AS INTERCONNECTION

Figure 4-3. Sequence of Events in Producing Gallium Arsenide Diode Array

The samples were then etched into individual mesas, each mesa being a diode. A layer of silicon dioxide was deposited on the diode mesas (by RF sputtering) and then etched to remove all the oxide except that which covered one of the sides of mesa. This oxide was used to prevent shorting out a diode when the interconnecting metal which formed the series connection between the diodes was applied. The final step was to evaporate silver on the sample, and etch to create the necessary interconnections. After the processing was completed and the array was diced from the substrate, the sample was mounted in a TO-5 header. The overall array is 0.1 inch by 0.1 inch.

Several major problems were faced in the design of this diode array. Problems that were solved included: precise etching of the GaAs-AlGaAs (both in terms of area and depth), and deposition of the silicon dioxide layer, which had to be deposited over a step.

A cross-sectional view of the diode array is shown in Figure 4-3. The diode array layout and mounting arrangements are shown in Figure 4-4.

## 4.2   DEVICE DESIGN PARAMETERS

In designing the first of these photodiode arrays, the problem was divided into three parts. Each part was considered separately, although there was considerable interaction between them. The three parts were: 1) the multilayer GaAs starting wafers, including the p-n junction and passivation layer, 2) the light capture area, and 3) the device conversion efficiency. Each of these is discussed below.

4.2.1   The GaAs starting wafers.

The technical approach to solving this problem was based on performing a set of experiments to determine the optimum growth conditions needed to produce the required resistivity, dopant impurity type, and layer thickness.

A matrix array of test growths were performed. Hall mobility measurements were made on these test samples to determine the optimum growth conditions. Hall measurements were used to determine sample resistivity and impurity levels, in addition to mobility. The mobility data gave a good indication of the purity of a grown layer. Therefore, the optimum conditions were defined as those conditions where the highest Hall mobility was obtained. Test growths to determine the optimum values were made using the JPL-built MOCVD reactor over a temperature range of 675° to 700° C, growth rates over the range of 40 to 200 nm per minute, dopant concentrations for Si (n-type) layers in the range of 2×10^{14} to 5×10^{18} cm^{-3}, and film layer thicknesses over the range from 10 nm to 3 µm.

For the JPL-built MOCVD system, the optimum growth temperature was found to be 700° C. At this temperature, a single undoped layer of GaAs had a Hall mobility of 60,000 at 60K. Therefore, 700° C was used to produce the GaAs layers for the photodiode array. In addition, the layers were doped with an impurity element. The tests indicated that layers as thick as 3 µm could easily be grown. For the photodiodes, thicknesses of 1.6 to 2.0 µm are needed with doping levels as high as 10^{18} cm^{-3}.
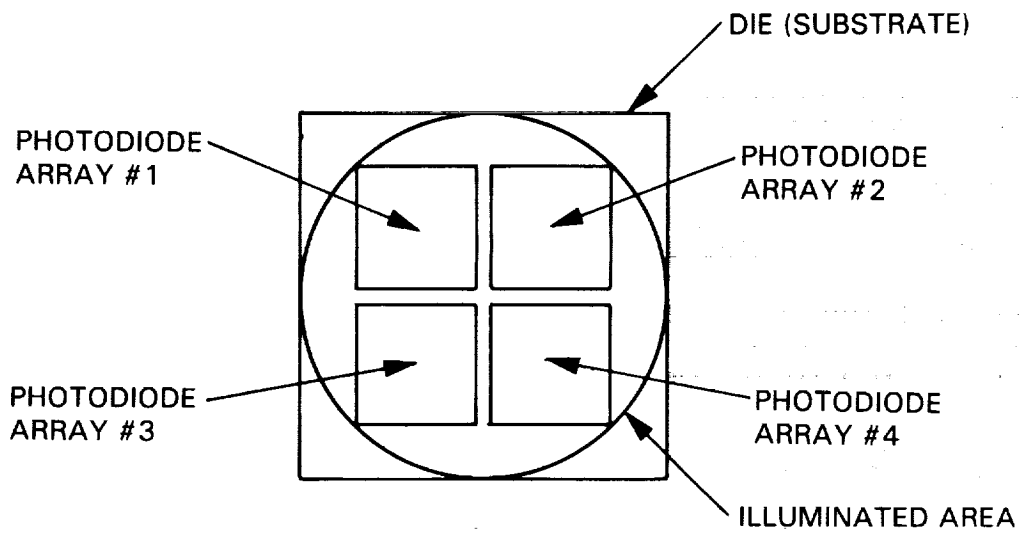
Figure 4-4. Diode Array Layout and Mounting Arrangements

The tests indicated that there was no problem making thick, heavily doped n-type layers of GaAs. However, problems were encountered when attempting to produce p-type layers. At this time, zinc-doped p-type layers with thickness of around 2 μm have not been consistently produced using the JPL MOCVD reactor because of doping gas problems. It is planned to try the Liquid Phase Epitaxial (LPE) reactor to grow the p-type layer. The LPE reactor has been successful in the past at growing p-type layers. Meanwhile, a new tank of zinc doping gas will be purchased for the JPL MOCVD.

After test structures (wafers) were made, the wafers were etched using standard photolithographic techniques. At first, some problems were encountered. The problems were caused mainly by equipment limitations, and were most acute when using the mask aligner. These problems were eventually solved by using a newer mask aligner with a higher resolution microscope.

Additional tests were made to determine the best method of dicing (cutting) the completed devices from the substrate wafer. This is always a problem when designing integrated circuits, especially when the circuits are made with GaAs. Each of the common methods of dicing was evaluated. These methods included: 1) laser scribing, 2) diamond scribing, and 3) diamond sawing. The results of these tests are given in Figures 4-5 through 4-9.

The damage seen on the cut edges in these photographs (Figures 4-5 through 4-9) probably propagates into the material. Therefore, the minimum distance from the edge (or scribe line) to the circuit is dependent on this damage. Using the method which produces the least amount of damage will allow a maximum of the die (chip) area to be used for the active circuits. Diamond scribing was determined to create the least amount of damage to the wafer, and therefore will be used as the dicing method.

In order to passivate the surface region of the photodiodes, AlGaAs was epitaxially grown on top of the p-n junction. This AlGaAs layer is basically transparent to 850 nm light, and helps to reduce surface recombination in the p-layer material, which decreases the overall efficiency of the photodiode.

4.2.2 Light Capture Area and Conversion Efficiencies

The size of the photodiode array was determined by the light source arrangement to be used. In this case, the light source feeding the photodiode array was a fiber optic cable. Figure 4-10 shows how the fiber optic cable feeds light to the photodiode array. A standard TO-5 IC header was chosen to be the device mount since it fits easily into a fiber optic connector. With the fiber not physically contacting the TO-5 header, but spaced away by a few millimeters, a fiber should be able to project light over most of the TO-5 device mounting area.

4-7

GaAs
WAFER

VIEWING
ANGLE

OBLIQUE   DIRECT   SAWED EDGE

POLISHED
SURFACE
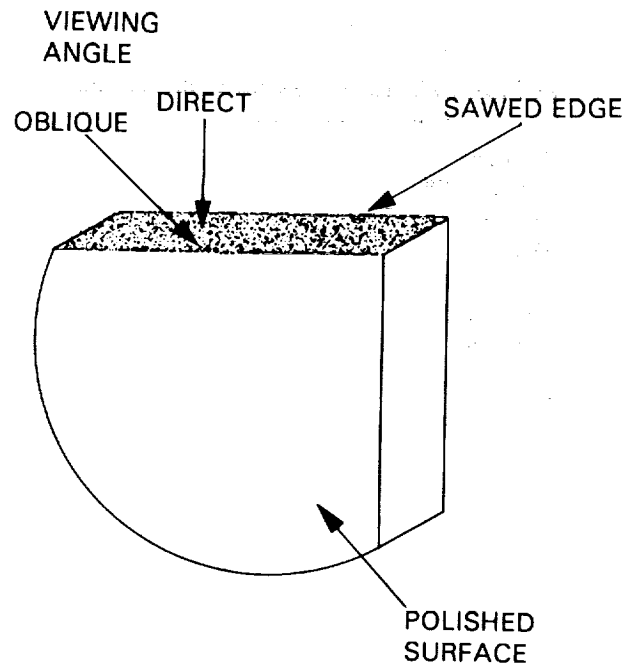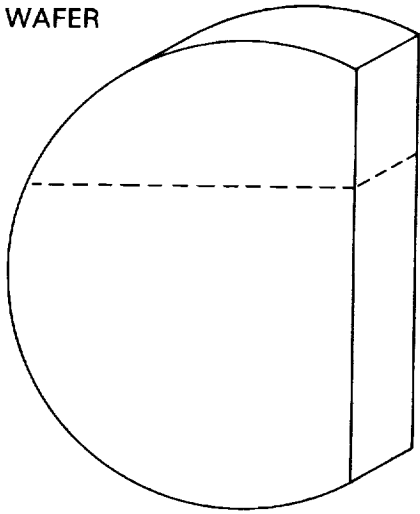
Figure 4-5. Gallium Arsenide Wafer Dicing, Showing Sawed Edge

Subsequent Scanning Electron Microscope (SEM) photographs of
diced wafers show the edge (or the corner) by either direct or
oblique-angle view
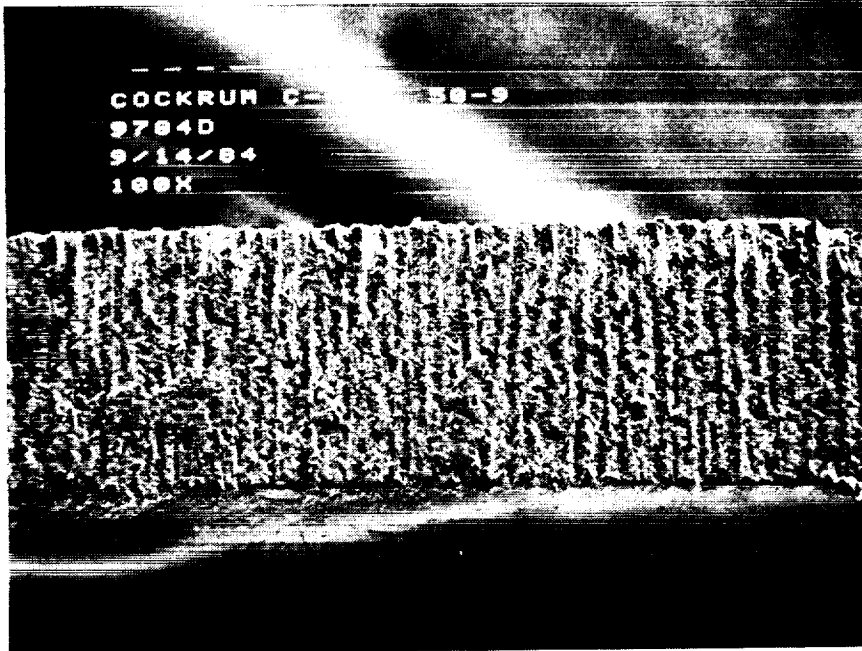
SEM HEADER

LASER
SCRIBED
SURFACE

POLISHED
SURFACE
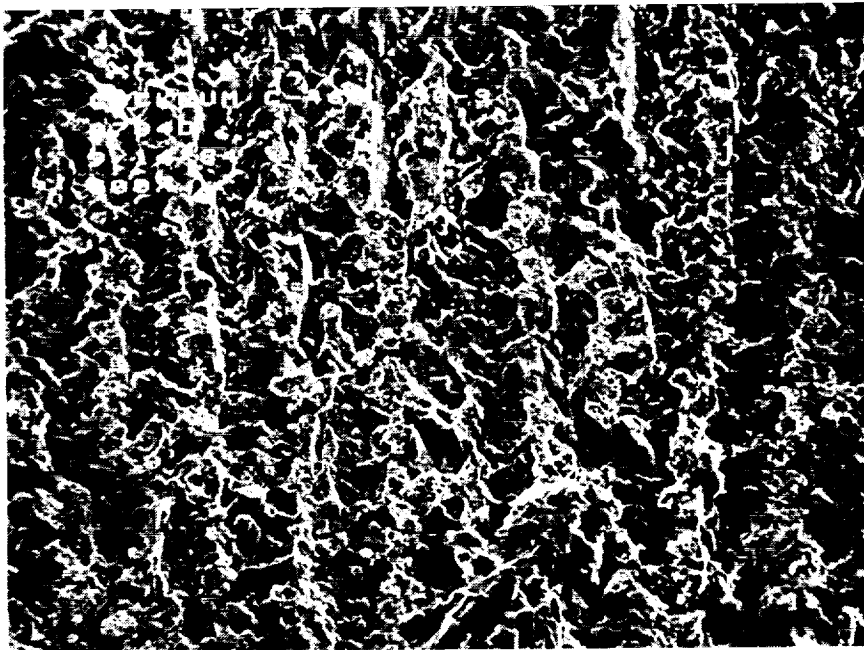
SCRIBED

SURFACE

Part of the polished surface of the wafer can be seen in (a): this is an oblique view. View (b) has 5 times the magnification of (a). Had the material been silicon the roughness of the surface would have disappeared because of local melting.

Figure 4-6. Two Views of a Laser-Scribed Gallium Arsenide Wafer

4-9
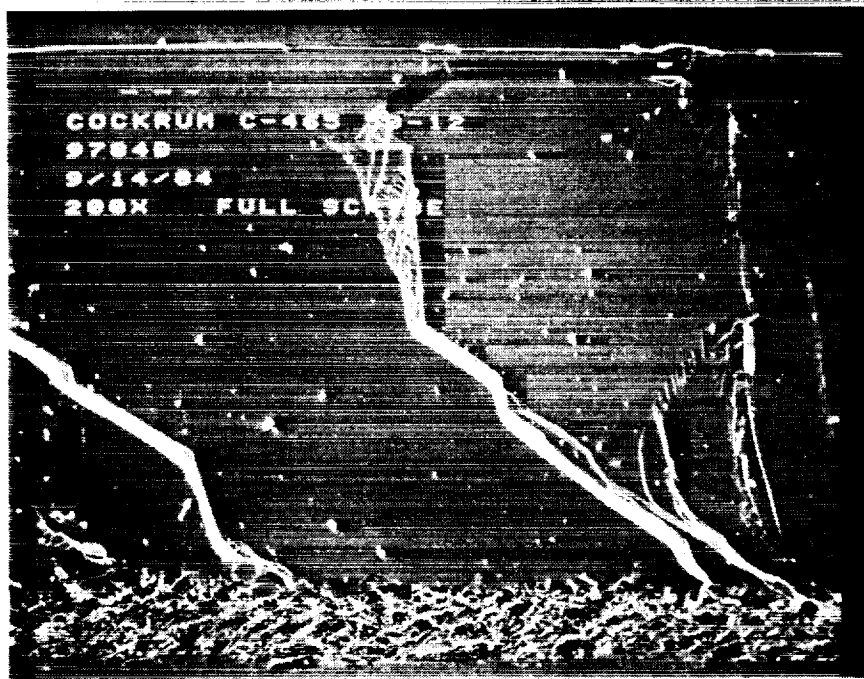
POLISHED
SURFACE

SCRIBED
SURFACE

Surface cracks can be seen propagating from the scribed surface
into the polished surface of the wafer.

Figure 4-7. Edge of Gallium Arsenide Wafer Scribed Side-to-Side

4-10

SEM HEADER

NON-SCRIBED CUT REGION — EDGE
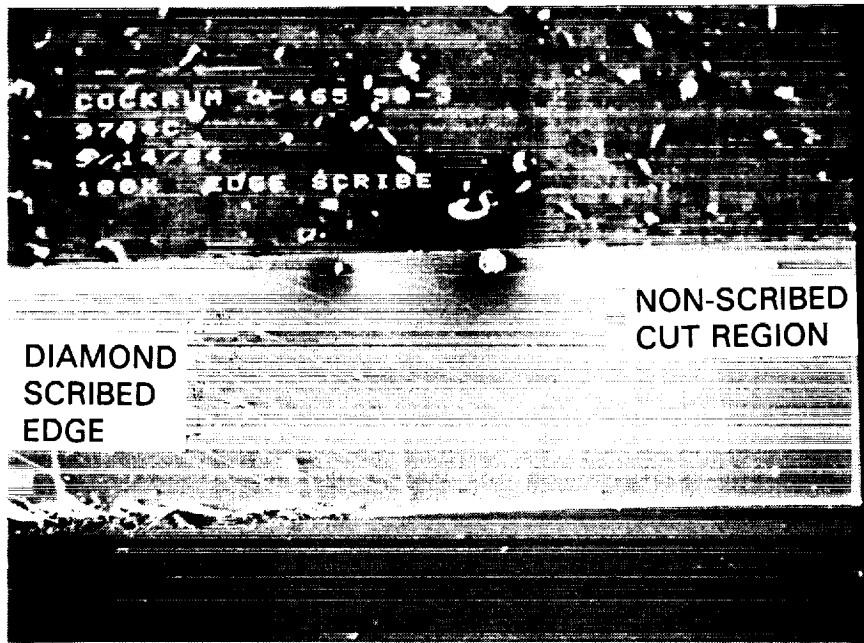
DIAMOND SCRIBED EDGE

POLISHED SURFACE

WAFER EDGE

POLISHED SURFACE

In this kind of dicing, only the corner of the wafer is scribed by the diamond. The wafer is then broken apart along a cleavage plane of the crystal. In (a) the damage caused by the scribe can be seen as surface cracks propagating into the photograph from the left. Further away from the scribed region, in (b), the edge can be seen to be smooth, and the corner between the edge and the polished surface is sharp.

Figure 4-8. Two Views of a Diamond-Scribed Gallium Arsenide Wafer

4-11

In (a) the cut surface seems to be smooth, but with more magnification, as in (b), roughness can be seen, and the corner with the polished surface is not sharp. Further, this method of dicing requires large separation between the circuits integrated on the wafer.

Figure 4-9. Two Views of a Gallium Arsenide Wafer Cut with a Diamond Saw

4-12

DEVICE

FIBER OPTIC
CABLE CONNECTOR

LIGHT

WIRES →

TO-5
HEADER

FIBER OPTIC
CABLE
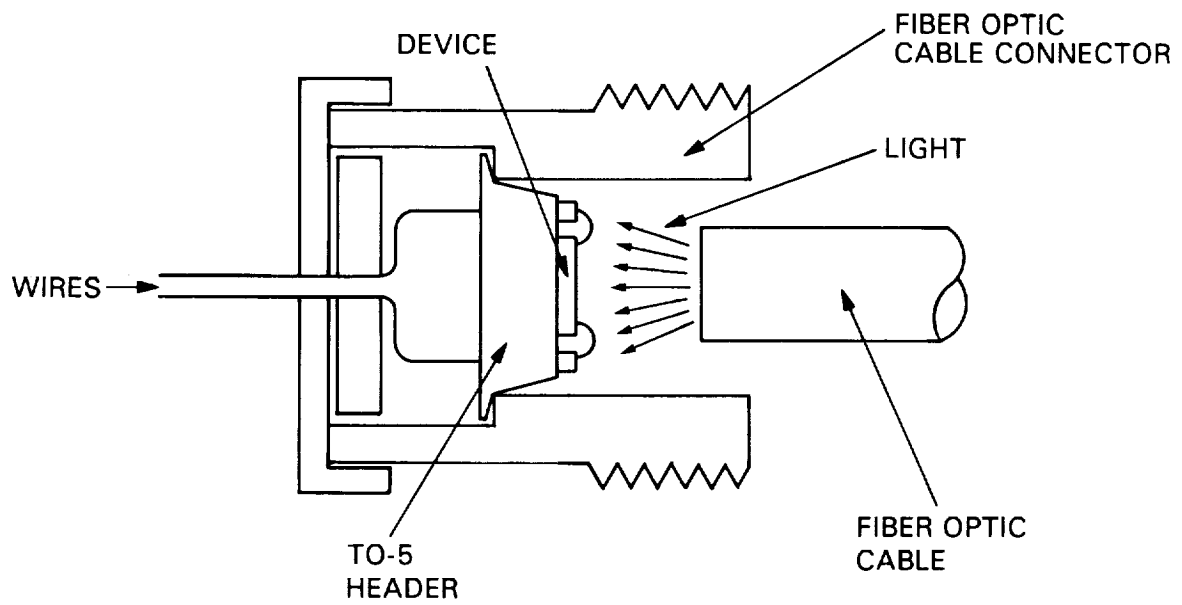
Figure 4-10. Photodiode Array Mounting Arrangement on Fiber Connector

The largest square device that can be mounted in a TO-5 header is 0.2 inches on a side. However, the photodiode array cannot be built all the way to the edge of the available area. Aside from the need for bonding pads (for connection to the outside), the act of cutting the circuit from the die damages the material at the edge. The array is therefore smaller than the available 0.2 by 0.2 inch area. The prototype design is approximately 0.07 inches on a side. A square of this size has a diagonal of 0.1 inch, so that 0.1 inch becomes the diameter of the smallest circle which will completely enclose the phototype array. Because the array is square, and the light emerging from a fiber can be assumed to illuminate a circular area, there is an effective loss of about 36%. Only 64% of the light in the circle is on the inscribed square. Once the lighted area is defined, an approximation of the device performance can be made.

It would be conservative to estimate that the conversion efficiency of a GaAs photodiode is equal to that of a typical silicon photodiode, such as those produced earlier as part of this project. A typical silicon photodiode has about 14% conversion efficiency. A higher conversion efficiency is expected for the GaAs photodiode array. A typical GaAs p-n junction cell conversion efficiency for monochromatic light is about 40%.

The light source will be assumed to project 100 mW onto the device. With 100 mW illuminating the circular region within which the square array is mounted, the active circuit area of the photodiode array sees 64 mW. Thus, the power available to be converted is 64 mW. If the array has 40% efficiency then 25 mW is delivered by the array. (These estimates do not account for any series resistance of the arrays, nor do they account for any degradation of performance when the device heats up.) The 'overall' efficiency of the system is thus on the order of 25%.

If the cells each produce about 0.75 volt (a very conservative estimate for GaAs), then the current per cell is 1 mA. It should be possible to produce ± 12 volts at 1 mA in a 32 diode array. This would power a reasonably large amount of electronics.

4.2.3 Device Fabrication.

As stated earlier in this report, all photodiodes will be produced using MOCVD or LPE techniques. These techniques have existed for about 10 years, but are still considered experimental. Standard GaAs IC etching techniques used with standard photolithography are used to produce the arrays. An actual etched array is shown in Figure 4-11.
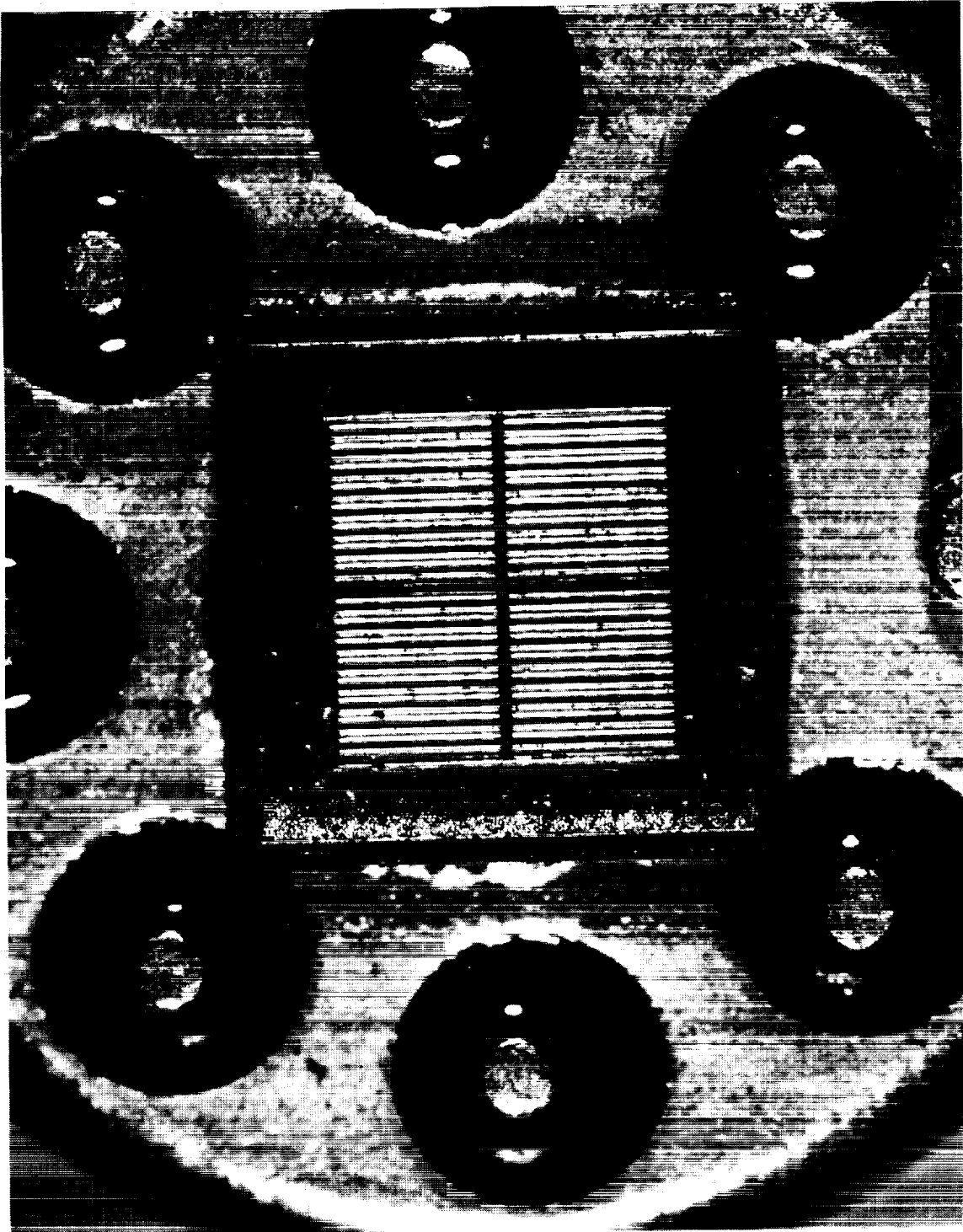
Figure 4-11. Photograph of 32-Diode Array

4.2.4 Test Results.

At this writing there are no test results from completed arrays. As stated earlier, problems with producing a 'good' p-layer, and alignment problems, have prevented making workable devices. Tests to determine the optimum growth conditions, and find solutions to the problems of p-layer growth, were performed, and results were presented earlier in this report.

4.3 Future Work.

After a workable device (array) is produced, and I-V curves made to determine conversion efficiency, studies will be conducted to determine the effects of heating (due to device dissipation), and to determine if the light level can be safely increased. Further, the question of lifetime and reliability of these devices will require study when a workable design has been established.

SECTION 5

CONCLUSIONS

This report has described work done at JPL on the Communications and Control for Electric Power Systems Project. The report reflects the emphasis placed by the project on the measurement of dc electric fields and the transfer of power over optical fibers.

At the time that this report was being finalized, tests were being carried out on the prototype of a miniaturized dc field sensor. This sensor is about a quarter of the diameter and half the length of the dc field probe described in this report. The electronics are packaged in a hybrid assembly on a ceramic substrate contained in a 0.6 inch diameter transistor can. Drive for the rotating components is by a modified dental-drill air turbine. The on-board electronics are powered by watch batteries, which are turned on by a centrifugally actuated switch at about 20,000 RPM. The electrodes are 0.75 inch in diameter and 1.5 inch long. Testing and evaluation of this instrument will continue in the coming year. The design, construction, and test results will be described in a separate report.

Gallium arsenide diodes have been produced singly (rather than in arrays) since this report was assembled. The first application of these diodes is planned to be in an ac field probe housed completely within a 2 cm sphere. These diodes and this field meter will also be described separately.

This report describes several methods of sensing distributed temperature. At the time of writing none of these have been experimentally tested. It is hoped to do so by 1987.
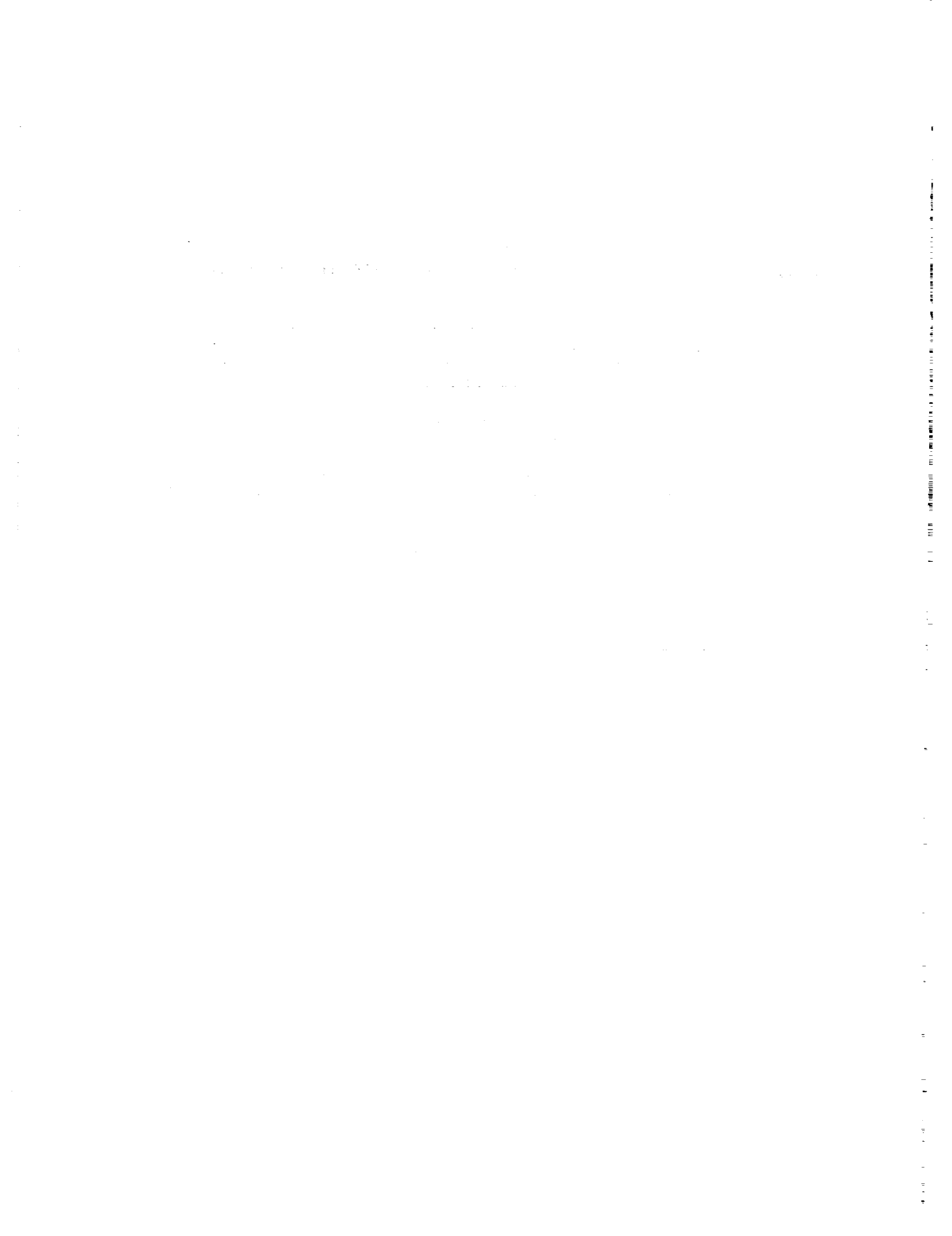
REFERENCES

Comber, M. G., and Johnson, G. B. (1982, July). HVDC Field and Ion Effects at Project UHV: Results of Electric Field and Ion Current Measurements. IEEE Trans. Power Apparatus and Systems, PAS-101 (7), pp. 1998-2006.

Comber, M. G., Kotter, R, and McKnight, R. (1983, November). Experimental Evaluation of Instruments for Measuring DC Transmission Line Electric Fields and Ion Currents. IEEE Trans. Power Apparatus and Systems, PAS-102 (11) pp. 3549-3557.

Deno, D. W. and Zaffanella, L. E. (1975). Electrostatic Effects of Overhead Transmission Lines and Stations. In Transmission Line Reference Book 345 kV and Above, Electric Power Research Institute, Palo Alto, CA, 1975.

Feser, K. and Pfaff, W. (1984, October). A Potential Free Spherical Sensor for the Measurement of Transient Electric Fields. IEEE Trans. Power Apparatus and Systems, PAS-103 (10), pp. 2904-2911.

Fox, R. (1983). Measurement of Peak Temperature along an Optical Fiber. Appl. Opt. 22 (7), pp. 967-969.

Hidaka, K. and Fujita, H. (1982, July). A New Method of Electric Field Measurements in Corona Discharge Using Pockels Device. J. Appl. Phys. 53 (9), pp. 5999-6003.

Kaune, W. T. and Phillips, R. D. (1980). Comparison of the Coupling of Grounded Humans, Swine and Rats to Vertical 60 Hz Electric Fields. Bioelectromagnetics, 1, 117

Kirkham, H., Johnston, A. R., Lutes, G., Daud, T., and Hyland, S. Power System Applications of Fiber Optics. Jet Propulsion Laboratory, Publication No. 84-28.

Maruvada, P. S., Dallaire, R. D., and Pedneault, R. (1983, March). Development of Field Mill Instruments for Ground Level and above-ground Electric Field Measurement under HVDC Transmission Lines. IEEE Trans. Power Apparatus and Systems, PAS-102 (3), pp. 738-744.

Misakian, M., S Kotter, F. R., and Kahler, R. (1978, July). Miniature ELF Electric Field Probe. Rev. Sci Instr. 49 (7), pp. 933-935.

Silva, M., Zaffanella, L., and Hummon, N. (1985, July). An Activity Systems Model for Estimating Human Exposure to 60 Hz Electric Fields. IEEE Trans. Power Apparatus and Systems, PAS-104 (7), pp. 1923-1929.

Takuma, T., Kawamoto, T, and Sunaga, Y. (1985, February). Analysis of Calibration Arrangements for AC Field Strength Meters. IEEE Trans. Power Apparatus and Systems, PAS-104 (2), pp. 489-496.

Wilhelmy, W. (1972). Floating Potential Field Strength Measurement in a Space Charge Free, Periodically Time Dependent and Transient Electric Field. Dissertation, University of Stuttgart. Available in English from University Microfilms, Ann Arbor, Michigan.